

2M4

Mr. J. F. Morris
Lewis

MEASUREMENT OF SINGLE CRYSTAL
SURFACE PARAMETERS

Final Report

NGR 38-010-005

Submitted to

National Aeronautics and Space Administration

Lewis Research Center

Cleveland, Ohio 44135

Submitted by

L. W. Swanson

A. E. Bell

R. W. Strayer

Linfield Research Institute

McMinnville, Oregon 97128

December 1972

(NASA-CR-137362) MEASUREMENT OF SINGLE
CRYSTAL SURFACE PARAMETERS Final Report
(Linfield Research Inst.) ~~77~~ p HC \$7.00
78

N74-20380

CSCL 20B

G3/26

Unclas
16649

MEASUREMENT OF SINGLE CRYSTAL
SURFACE PARAMETERS

Final Report

NGR 38-010-005

Submitted to

National Aeronautics and Space Administration

Lewis Research Center

Cleveland, Ohio 44135

Submitted by

L. W. Swanson

A. E. Bell

R. W. Strayer

Linfield Research Institute

McMinnville, Oregon 97128

December 1972

I

ABSTRACT

The sticking coefficient and thermal desorption spectra of Cs from the (110) plane of W has been investigated. A sticking coefficient of unity for the monolayer region was measured for $T < 250^{\circ}\text{K}$. Several distinct binding states were observed in the thermal desorption spectrum.

Work function and electron reflection measurements were made on the (110) and (100) crystal faces of Mo. Both LEED and Auger were used to determine the orientation and cleanliness of the crystal surfaces. The work function values obtained for the (110) and (100) planes of Mo were 4.92 and 4.18 eV respectively.

Table of Contents

Abstract.....	i
Cesium Adsorption and Desorption From the (110) Plane of Tungsten	
I. Introduction.....	1
II. Experimental.....	3
Tube Design and Preparation.....	3
Dose Rate Calibration.....	5
Desorption Detection and Sensitivity.....	6
Sticking Coefficient Measurements.....	7
Thermal Desorption Measurements.....	9
III. Data and Discussion.....	11
Sticking Coefficient.....	11
Thermal Desorption.....	14
Table I.....	16
IV. Conclusion.....	17
V. References.....	19
VI. Figure Titles.....	20
Figures 1-10.....	21
Work Function and Electron Reflection Measurements From the (110) and (100) Planes of Molybdenum	
I. Introduction.....	31
II. Theoretical Considerations.....	34
III. Electron Reflection.....	37
IV. Experimental.....	38
Crystal Preparation: Polishing, Mounting and Laue Patterns.....	38
Crystal Cleaning: LEED Auger Techniques.....	39
Work Function, Reflection Measurements.....	41

V.	Experimental Results.....	43
	Laue Results.....	43
	LEED Results.....	44
	Auger Results.....	45
	Vacuum Environment for Work Function and Electron Reflection Measurements.....	46
	Work Function Results.....	46
	Electron Reflection Results.....	46
IV.	Discussion.....	48
	Work Function Values.....	48
	Surface Impurity Concentration Estimates.....	49
	Reflection Coefficients.....	51
	Table I.....	54
VII.	References.....	55
VIII.	Figure Titles.....	57
	Figures 1-15.....	59

Cesium Adsorption And Desorption From The (110) Plane Of Tungsten

I. INTRODUCTION

The adsorption and desorption of cesium on polycrystalline tungsten surfaces have been studied by numerous authors using a variety of techniques.¹⁻⁶ The desorption kinetics discussed in these studies are greatly complicated by the multiplicity of adsorption states, the variation of binding energy with coverage and crystal direction, and the complicated dependence of the averaging of desorption rates from different crystal faces on the degree of adsorbed atom mobility. Desorption studies on macroscopic single crystals should help to remove some of the complications listed above and thus improve the comparison of results with theoretical models.

At present there exists little reliable thermal desorption and sticking coefficient data for Cs on macroscopic single crystal W surfaces. The preliminary work reported here is an attempt to provide such data for Cs on the (110) surface of W by means of an extension of the field emission detection method developed by Bell and Gomer⁷ to study CO adsorption on W. The major significance of this method is that desorption products and sticking coefficients are determined from the amount of cesium reflected rather than the amount adsorbed. Because of the extremely small size of the field emitter used as a detector and its high sensitivity, desorption or reflection from

a very small section of the center of a macroscopic crystal surface contribute greatest to the detector, thereby reducing undesirable edge effects. This method also reduces the effect of concomitant diffusion to the backside of the target crystal during desorption, which can confuse measurements when large area detectors are employed.

II. EXPERIMENTAL

Tube Design and Preparation

A diagram of the experimental tube is given in Fig. 1. It may be divided functionally into several parts: (a) Cs reservoir, (b) reproducible Cs evaporative source, (c) detector assembly, (d) target crystal, and (e) dose measuring ring.

The Cs reservoir is an aluminosilicate glass ampule containing Cs purchased from A. D. MacKay Co. and vacuum distilled in a separate operation. After being attached to the experimental tube, the interior tip of the glass ampule is broken as the last step in the evacuation of the experimental tube, allowing a small residual amount of gas to be pumped away. By immersing the entire tube in liquid nitrogen the Cs vapor pressure is kept negligible.

By heating the Cs reservoir, Cs may be condensed onto a resistively heatable Pt disk, which is the evaporative source for the target. The disk is mounted on a four-wire filament connected to an accurate heating circuit, so that a controlled amount of Cs may be deposited on the target. One loading of the Pt disk provides a satisfactory source for a larger number of controllable and reproducible doses of Cs.

The detector is a (110)-oriented W field emitter attached to a filament

mounted on a slide assembly. By means of an external electromagnet the emitter can be positioned either down in front of the target in line with the source or up in front of a phosphor screen. In the down position the emitter tip is shielded by the emitter blank from direct Cs deposition from the source; only Cs atoms reflected or desorbed from the target can reach the tip. In the up position the field emission pattern formed on a phosphor screen may be viewed and current-voltage data taken without affecting the target coating.

The target crystal is a circular disk 5.2 mm in diameter and 0.4 mm thick. It was fabricated from a Marz Grade zone-melted single crystal (110) -oriented W rod purchased from Materials Research Corporation. The target surface was polished by electrochemical machine etching. The surface is single crystal and has a normal oriented to within one degree of the (110) direction, as verified by Laue back-scattered X-ray patterns. The target crystal is mounted on a 4-wire filament so that its temperature may be controlled by the usual resistive heating and potential sampling techniques. Temperature calibration was accomplished by measuring the resistance of the target at liquid nitrogen, room and pyrometric temperatures, then utilizing the monotonic relation between temperature and the resistivity of W for interpolation.⁸ For the most part temperatures were below the point where radiative corrections were necessary and pyrometric measurements showed less than 10° variation across the

crystal at 1200^o K.

The dose measuring ring is a 0.4 mm D W ring located behind the target but visible to the Cs source. Its purpose is to provide a relative measurement of the number of Cs atoms striking the target during adsorption.

Dose Rate Calibration

Knowledge of the amount of Cs deposited on the target surface is important both in the determination of sticking coefficient as a function of Cs coverage and in the study of desorption. For this purpose the difference between the work function of the (110) W surface (5.3 eV) and the ionization potential of Cs (3.9 eV) was utilized to convert the atom beam from the Cs source into an ion current through surface ionization. The target was heated to 1000^oK, a temperature for which an ion current of about 10^{-8} amp was supply-limited rather than temperature-limited and for which the fraction of neutral atoms leaving the target was negligible (these conclusions were verified by measuring ion current as a function of temperature and noting that it remained constant for small variations in temperature in the neighborhood of 1000^oK). The ion current was collected at a tube wall potential of -100 V relative to the target. It was independent of applied voltage between 20 and 300 V, thus showing space charge and secondary emission effects were negligible; under these conditions the dose rate is determined

from the relationship

$$\frac{\sigma}{t} = \frac{I_t}{eA}, \quad (1)$$

where σ is the number of Cs atoms per unit area of the target crystal, t is the time, I_t is the ion current, e is the electronic charge, and A is the area of the target. For an ion current of 10^{-8} amp, $\sigma/t = 2.9 \times 10^{11}$ atoms/cm² - sec for the target used in this experiment.

When the target is at low temperature, the dose rate is determined by means of the dose measuring ring. It is calibrated by measuring the ratio I_r/I_t , where I_r is the ion current from the ring, when both ring and target are at 1000°K.

Desorption Detection and Sensitivity

The desorption or reflection of Cs from the target crystal was monitored by noting the change in the field-emission current-voltage relationship of the emitter detector. The amount of Cs reaching the detector was determined from the relationship between emitter work function and Cs coverage previously established by Swanson and Strayer⁹ for Cs on W. One should be able to relate coverage on the emitter detector to the amount desorbed from the target by assuming isotropic desorption (i. e., all directions within a solid angle of 2π are equally probable). Thus the ratio of emitter coverage σ_e to the change in target coverage $\Delta\sigma$ is

$$\sigma_e / \Delta \sigma = \frac{1}{2\pi} \int_{\Omega} d\Omega = \frac{1 - R/r}{\sqrt{1 + (R/r)^2}} \quad (2)$$

where R is the target-to-detector spacing and r is the target radius; and, for R = 2.2 mm and r = 2.6 mm, we get $\sigma_e / \Delta \sigma = 0.35$. In practice, this approach was not reliable, probably due to the different bias voltages that must be placed on other tube elements to distinguish between atom and ion desorption. Instead we measured the amount of Cs adsorbed, as described in the previous section, and used the total amount reaching the detector during a complete desorption sequence to establish a desorption-adsorption ratio, which was then applied to the individual desorption steps. That concomitant diffusion of Cs to the back side of the target during desorption was not a problem was proven by verifying that the size of the temperature steps during desorption had no effect on the amount desorbed. One of the most important advantages of this technique is its extreme sensitivity of detection. The field emission current I is related to work function ϕ and field strength F by the well known Fowler-Nordheim equation, which can be written

$$I = 1.54 \times 10^{10} \frac{AF^2}{\phi t(y)} \exp \left[0.68 \phi^{3/2} v(y)/F \right] \quad (3)$$

where A is the emitting area in cm^2 , F and ϕ are in units of $\text{V}/\text{\AA}$ and eV,

respectively, and the image correction terms $t(y)$ and $v(y)$ are slowly varying tabulated ¹¹ functions of the auxiliary variable $y = (e^3 F)^{1/2} / \phi$, and have the approximate values of 1.04 and 0.73, respectively. Thus one can show easily that

$$\frac{dI}{I} = 0.74 \frac{\phi^{3/2}}{F} \frac{d\phi}{\phi} \quad (4)$$

Since fractional monolayer coverage is a linear fraction of ϕ at low coverage, Eq. (4) may be rewritten

$$\frac{dI}{I} = 0.74 \frac{b\phi^{1/2}}{F} \frac{dN}{N_0} \quad (5)$$

where N_0 is the monolayer adsorbate density and $b = 2 \mu N_0$. The adsorbate dipole moment μ directly controls the sensitivity of $\frac{dI}{I}$ with respect to $\frac{dN}{N_0}$. For Cs on W, $b = 13$ eV and $\frac{\phi^{1/2}}{F} = 7$ for typical emission levels; ⁹ thus

$$\frac{dI}{I} = 67 \frac{dN}{N_0} \quad (6)$$

Assuming a 1% change in current is measurable, we find that $dN/N_0 = 1.5 \times 10^{-4}$. This is very nearly single atom sensitivity over the emitting area of the field emission detector.

Sticking Coefficient Measurements

Sticking coefficient data was obtained in the following manner: First the ion current for the proper dose rate was determined as outlined previously. The target crystal was then cleaned by resistive heating.

The field emission tip was then flashed clean and while in the raised position a reference series of current-voltage measurements taken. The tip was then allowed to drop in front of the target crystal, the target heated to the desired temperature, and the dosing platform heated to drive a pre-selected amount of cesium onto the surface of the target crystal. This amount was usually about 0.2×10^{14} atoms/cm². The tip was then raised and current-voltage measurements taken to determine if there had been a change in the work function of the tip indicating the presence of cesium on it. The tip was then flashed clean and another reference run made. This process was repeated until the total coverage of cesium on the target crystal was about 5×10^{14} atoms/cm². After this the target crystal was again cleaned by heating so that another run at another target temperature could be made. This heating process was usually done in steps so that the amount of cesium desorbed at this time could be compared with the amount deposited.

Thermal Desorption Measurements

The method employed here to investigate thermal desorption involves heating the single crystal substrate in small time increments to increasing temperatures after multilayer adsorption. By examining the amount desorbed after each heating period a plot of amount desorbed vs. desorption temperature can be obtained. Existence of specific binding states can be ascertained from this plot. This process in effect constitutes a slow motion

flash desorption with much larger resolution and sensitivity than obtainable with commonly used pressure or mass spectrometer detection devices.

The desorption spectrum of cesium from tungsten (110) was obtained as outlined below: After a surface density of approximately 5×10^{14} atoms/cm² had been adsorbed on the target crystal while it was at a temperature of 77°K it was heated for ten second intervals with the emitter in the down position and biased 100 V positive with respect to the target crystal. This was to insure that only cesium neutrals were measured at the emitter. After each heating period the amount of cesium desorbed was measured as described previously and the process repeated at increased substrate temperature until no further desorption was observed.

This series of measurements was also taken without the bias voltage and with the emitter biased at about 23.5 V negative with respect to the target crystal so that ions could be collected at the emitter. Ionic desorption rates were then obtained by subtracting the neutral desorption rate from that of neutrals and ions.

III. DATA AND DISCUSSION

Sticking Coefficient

Measurements of the sticking coefficient as a function of target coverage were taken at target temperature of 77°K, 200°K, 250°K and 300°K; the resulting curves are presented in Figure 2. For these measurements the sticking coefficient α_s is defined as

$$\alpha_s = 1 - \frac{n_r}{n_i} \quad (7)$$

where n_r is the number of reflected atoms and n_i is the number of incident atoms.

The first thing to note about the data displayed in Figure 2 is that α_s is unity from zero to multilayer coverage for temperatures of 250°K and below. Because the unity value of the sticking coefficient extends to multilayer coverages we may also conclude that the self-condensation coefficient for Cs at temperatures up to 250°K must also be near unity. One major significance of these results is that they support the assumption that $\alpha_s = 1$ used by everyone since Langmuir¹ to calculate the experimental σ vs. θ relationship for Cs on W.

The large value of α_s observed experimentally for Cs on W is probably due to the large value of binding energy at low coverage and to the fairly good

match between the masses of W and Cs atoms. The importance of the latter point comes from a consideration of the accommodation coefficient α_a which measures the efficiency of energy transfer and is usually defined as

$$\alpha_a = \frac{E_r - E_i}{E_s - E_i}, \quad (8)$$

where E_i , E_r and E_s are the energies of the incident, reflected and surface atoms, respectively. If $\alpha_s = 1$ it follows that α_a must also be unity.

Straight forward application to the laws of conservation of momentum and energy to the collision of the incident atoms with the surface atoms leads to the relationship

$$\alpha_a = \frac{2mM}{(m+M)^2}, \quad (9)$$

where m and M are the masses of the two particles involved in the collision.

The maximum of α_a ($\alpha_a = 0.50$) is obtained when the masses of the two particles are equal; W and Cs atoms equation (9) leads to a value of $\alpha_a = 0.49$.

At a target temperature of 300° K, the sticking coefficient goes to zero at a coverage of 6.58×10^{14} atoms/cm² (Figure 2) this is due to concomitant thermal desorption. The variation of α_s with coverage has treated theoretically;¹²⁻¹⁴ Kisliuk's model,¹² as generalized by Kuhrt and Gomer,^{14, 15}

seems applicable to our data. For nondissociative adsorption on a single site,¹⁵

$$\alpha_s(\theta) = \alpha_s(\theta) \left[1 + K \frac{\theta}{1-\theta} \right]^{-1}$$

where θ is defined in this case as

$$\theta = \sigma / \sigma_{\max}, \quad (11)$$

and K has the meaning¹⁵

$$K = \frac{P'_d}{P_e + P_d} \quad (12)$$

where P_e and P_d stand for the probabilities of adsorption and desorption, respectively, and the unprimed quantities refer to an empty site and the primed one to a filled site. The curve in Figure 2 is equation (10) with K chosen to provide a best fit to the 300°K data; the value of K required is 0.02. If the surface processes may be broken up into distinct adsorption, desorption and diffusion steps, Kuhrt and Gomer have shown¹⁵ that K may be written

$$K = \frac{K'_d K_{\text{dif}}}{K_{\text{dif}}' K_a} \quad (13)$$

where the K 's are the rate constants for the indicated processes. Since it has been determined¹⁶ that $K_{\text{dif}} / K_{\text{dif}}' > 1$ for Cs on W, $K=0.02$ implies

that $K'_d \ll K_a$ and thus that $E_a < E'_d$, where the E's are the activation energies for the two processes.

Thermal Desorption

The desorption spectra for Cs on (110)W are shown in Figures 3 and 4 for Cs adsorbed at two different target temperatures, 77°K and 300°K. The difference in peak heights, between 300 and 400°K for the two spectra is due to a difference in the total amount adsorbed; otherwise the two spectra are quite similar. Three more or less distinct states may be ascertained, one with a peak at ~ 350°K, one with a peak at ~ 550°K and one with a peak at ~ 1000°K. Assuming first order kinetics apply,

$$\frac{d\sigma}{dt} = -k_a \sigma, \quad k_a = \nu e^{-E_a / kT} \quad (14)$$

where k_a is the atomic rate constant, ν a pre-exponential factor with the dimensions of frequency, E_a the atomic desorption energy, k and T are Boltzmann's constant and target temperature, respectively, an equation, relating atomic desorption energy to Cs coverage may be derived:

$$E_a(\sigma) = kT \ln \left(\nu t \frac{1}{\ln \sigma_i / \sigma_t} \right), \quad (15)$$

where σ_i and σ_f are the initial and final coverages obtained when heating the target to a temperature T for a time period t . Using the data of Fig. 3 plotted in the form of the amount remaining as a function of desorption

temperature (Figure 5) and assuming $\nu = 10^{12} \text{ sec}^{-1}$, $E_a(\sigma)$ is calculated from eq. (15) and graphed in Figure 6, where the horizontal bars represent coverage increments. Also graphed for comparison are the results obtained by Swanson et al.² for polycrystalline W.

The flat portion of the curve between 2.0 and $4.0 \times 10^{14} \text{ atoms/cm}^2$ is apparently due to the emptying of a loosely bound state of constant binding energy consisting of second and partial first layer Cs. The portion of the curve between inflection points at 0.4 and $1.4 \times 10^{14} \text{ atoms/cm}^2$ is probably due to another adsorption state where binding energy is less well defined than that of the higher coverage state. For $\sigma < 0.4 \times 10^{14} \text{ atoms/cm}^2$, a third state appears with a very high binding energy, and as σ approaches zero the value of E_a approaches 3.5 eV . This value of E_a at terminal coverage is somewhat higher than expected. This could possibly be due to the presence of a small amount of oxygen in the tube. Similar results could also be obtained if the desorption period of ten seconds is not long enough to remove all of the cesium that would normally come off at a given temperature. Although the values of activation energy are higher than those obtained elsewhere the general shape of the curve agrees very well with those of others.²

In order to verify the validity of the use of the first order rate equation eq. (14) to describe the thermal desorption results, the variation of σ with t at constant T was examined in the coverage interval 5 to $2.1 \times 10^{14} \text{ atoms/cm}^2$.

This coverage interval covers the low temperature (350°K) desorption peak of Figs. 3 and 4. By rewriting eq. (15) in the form

$$\ln \frac{\sigma_i}{\sigma_a} = k_a t \quad (16)$$

and plotting $\ln \sigma$ vs. t a straight line with slope of k_a should be obtained. The results given in Fig. 7 indicate three separate straight line segments. This result, in turn, suggests the presence of three distinct sub-desorption states within the low temperature peak of Figures 3 and 4. Values of k_a and E_a obtained in this coverage interval from the slopes of the 3 straight line segments of Fig. 7 are given in Table I assuming, as before, $\nu = 10^{12} \text{ sec.}^{-1}$

TABLE I
Figure 7 Results Assuming $\nu = 10^{12} \text{ sec.}^{-1}$

Region	k_a (sec. ⁻¹)	E_a (eV)	$\Delta \sigma$ ($\times 10^{14}$ atoms/cm ²)
1	1.18×10^{-2}	0.802	5.1 - 4.7
2	8.20×10^{-4}	0.868	4.7 - 2.3
3	3.52×10^{-5}	0.946	2.3 - 2.1

These distinct desorption states are attributed to geometric arrangements of the ad-layer which alter the binding forces. The region 3 state, exhibiting a binding energy near that of the heat of sublimation of bulk Cs, is probably due to true multilayer desorption.

Ionic desorption rates were studied by removing the bias voltage between the emitter and target and also by biasing the emitter at about 23.5 v. negative with respect to the target crystal so that ions could be collected. It was later felt that the presence of this bias could have adversely affected the measurements and they were not considered further. The results obtained without a bias are shown graphically in Figures 8-10.

The heat of ionic desorption E_p is theoretically related to the heat of atomic desorption E_a , in the absence of applied field, by the equation

$$E_p = E_a + I - \phi \quad (17)$$

where $I = 3.9$ eV and is the ionization potential of cesium. At low coverages where $\phi > I$ it is evident from equation (17) that $E_p < E_a$ in other words the desorption will occur mostly as ions. Using our terminal coverage values of $E_p = 2.0$ eV and $E_a = 3.5$ eV equation (17) leads to a value of $\phi = 5.4$ eV which is very close to the value of 5.3 eV usually reported for the (110) plane of tungsten. To date, attempts to obtain ionic desorption energies by subtraction from those of combined ions and neutrals have not been successful.

IV. CONCLUSION

These results point out the usefulness of this technique to obtain a variety of surface kinetic parameters for an adsorbate - substrate system. For example, sticking coefficients, binding energies, and desorption spectra can be obtained from a single experimental tube. The results show

that cesium is adsorbed on W(110) in discrete binding states throughout the coverage range.

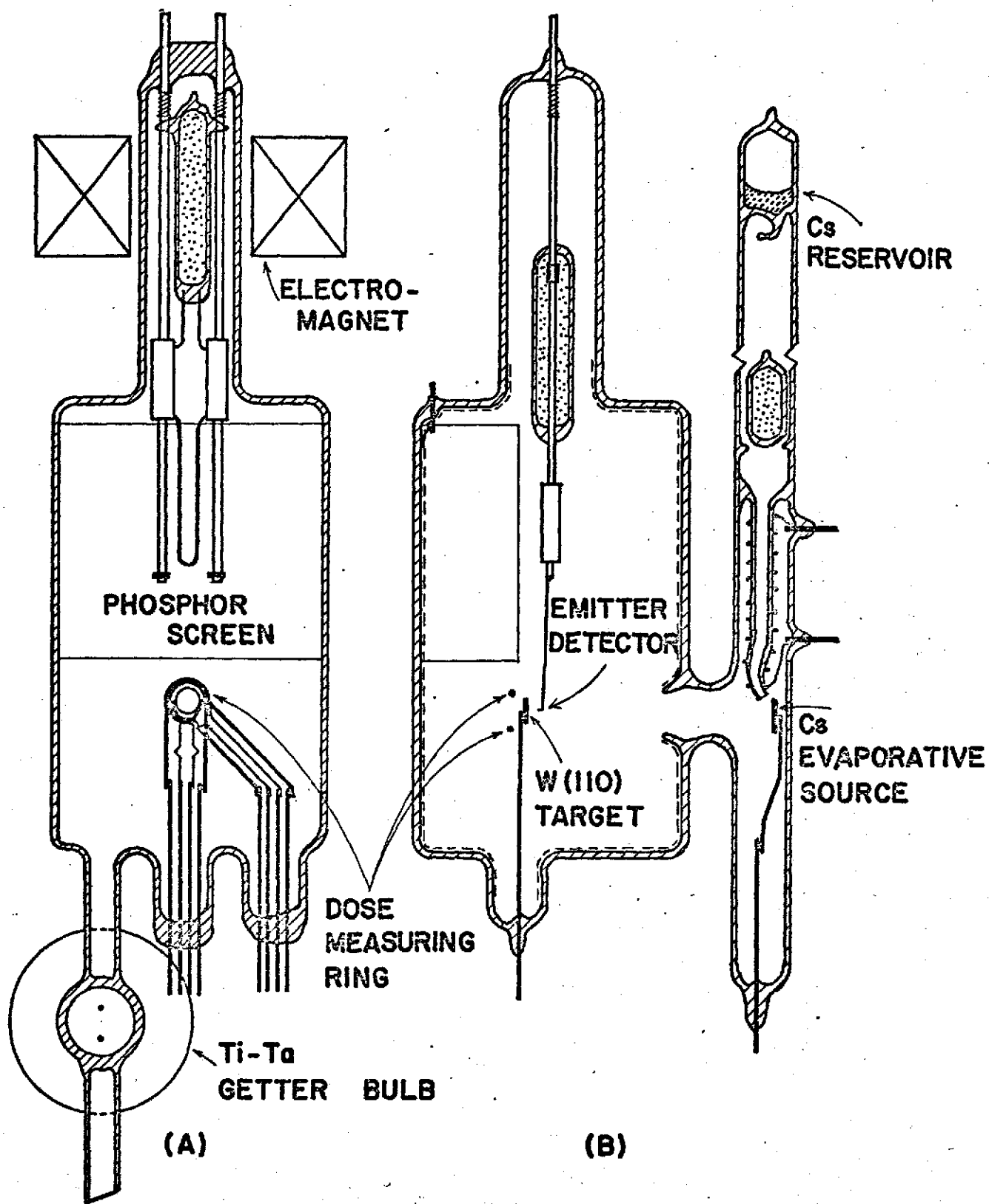
V. REFERENCES

1. J. B. Taylor and I. Langmuir, *Phys. Rev.* 44, 423 (1933).
2. L. W. Swanson, R. W. Strayer, E. C. Cooper, and F. M. Charbonnier, Annual Report on NASA Contract Nr. NASw-458 (1963); L. W. Swanson, R. W. Strayer, C. J. Bennette, and E. C. Cooper, Final Report on NASA Contract NAS 3-2596 (1964).
3. I. Langmuir and K. H. Kingdon, *Proc. Roy. Soc. (London)* A107, 61 (1925).
4. M. J. Copley and T. E. Phipps, *Phys. Rev.* 48, 960 (1933).
5. S. Datz and E. H. Taylor, *J. Chem. Phys.* 25, 389 (1956).
6. M. D. Scheer and J. Fine, *J. Chem. Phys.* 37, 107 (1962).
7. A. Bell and R. Gomer, *J. Chem. Phys.* 44, 1065 (1966).
8. Colen J. Smithells, Tungsten: Its Metallurgy, Properties and Applications (Chemical Publishing Co Inc., New York, N.Y., 1953), 117.
9. L. W. Swanson and R. W. Strayer, *J. Chem. Phys.* 48, 2421 (1969).
10. R. Gomer, Field Emission and Field Ionization, (Harvard University Press, Cambridge, Mass., 1961).
11. R. H. Good, Jr. and E. W. Müller in Handbuch der Physik (Springer, Berlin, 1965), 21, 176.
12. P. Kisliuk, *J. Phys. Chem. Solids* 3, 95 (1957); 5, 78 (1958).
13. G. Ehrlich, *J. Phys. Chem. Solids* 5, 47 (1958).
14. C. Kohrt and R. Gomer, *J. Chem. Phys.* 52, 3283 (1970).
15. C. Kohrt and R. Gomer, *Surf. Sci.* 24, 77 (1971).
16. L. W. Swanson, R. W. Strayer, F. M. Charbonnier, and E. C. Cooper, in Electric Propulsion Development (vol. 9 of "Progress in Astronautics and Aeronautics"), ed. by Ernst Stahlinger. (Academic Press, New York, 1963), p. 165.

VI. FIGURE TITLES

- Figure 1. Diagram of experimental tube. (A) Front view with the emitter detector in the "up" position. (B) Side view with emitter detector in the "down" position.
- Figure 2. Sticking coefficient as a function of Cs surface coverage for several target temperatures. The solid curve fitting the 300°K data is a Kisliuk isotherm with $K = 0.02$ (see text).
- Figure 3. Desorption spectra for neutral Cs atoms ($\sigma = 4.2 \times 10^{14}$ atoms/cm², $T = 77^\circ\text{K}$ for adsorption).
- Figure 4. Desorption spectra for neutral Cs atoms ($\sigma = 6.6 \times 10^{14}$ atoms/cm², $T = 300^\circ\text{K}$ for adsorption).
- Figure 5. Plot of the amount remaining vs. desorption temperature for data of Fig. 3 (neutrals).
- Figure 6. Plot of the atomic desorption energy as a function of Cs coverage for Cs on (110)W. The dashed curve is for Cs on polycrystalline W, from Swanson et al.²
- Figure 7. Plot of cesium coverage vs. time at a constant desorption temperature of 290°K.
- Figure 8. Desorption spectra with target biased to permit desorption of both Cs neutrals and ions ($\sigma = 5.2 \times 10^{14}$ atoms/cm², $T = 77^\circ\text{K}$ for adsorption).
- Figure 9. Plot of amount remaining vs. desorption temperature (neutrals + ions).
- Figure 10. Plot of desorption energy vs. Cs coverage on (110)W (neutrals + ions).

Figure 1



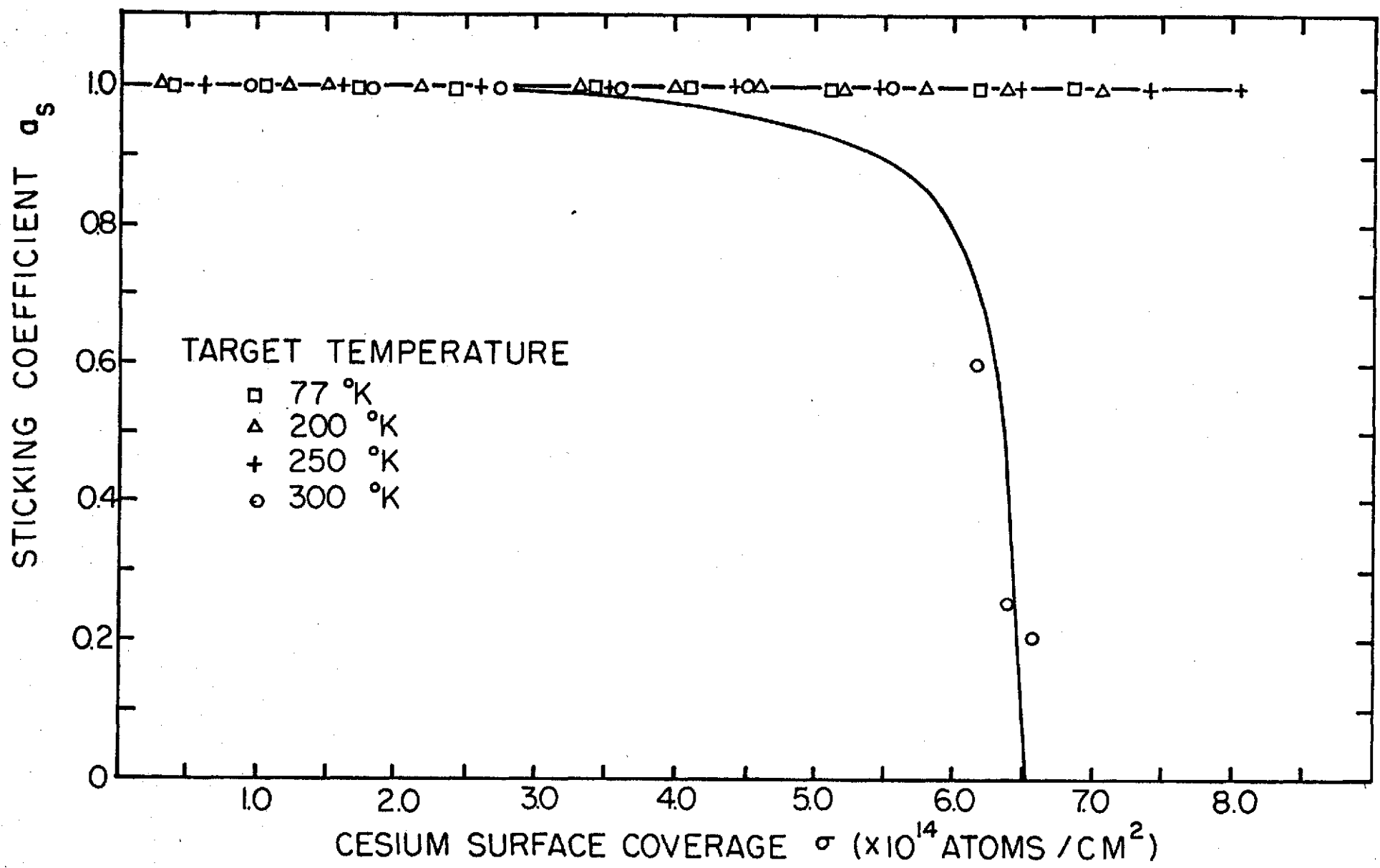


Figure 2

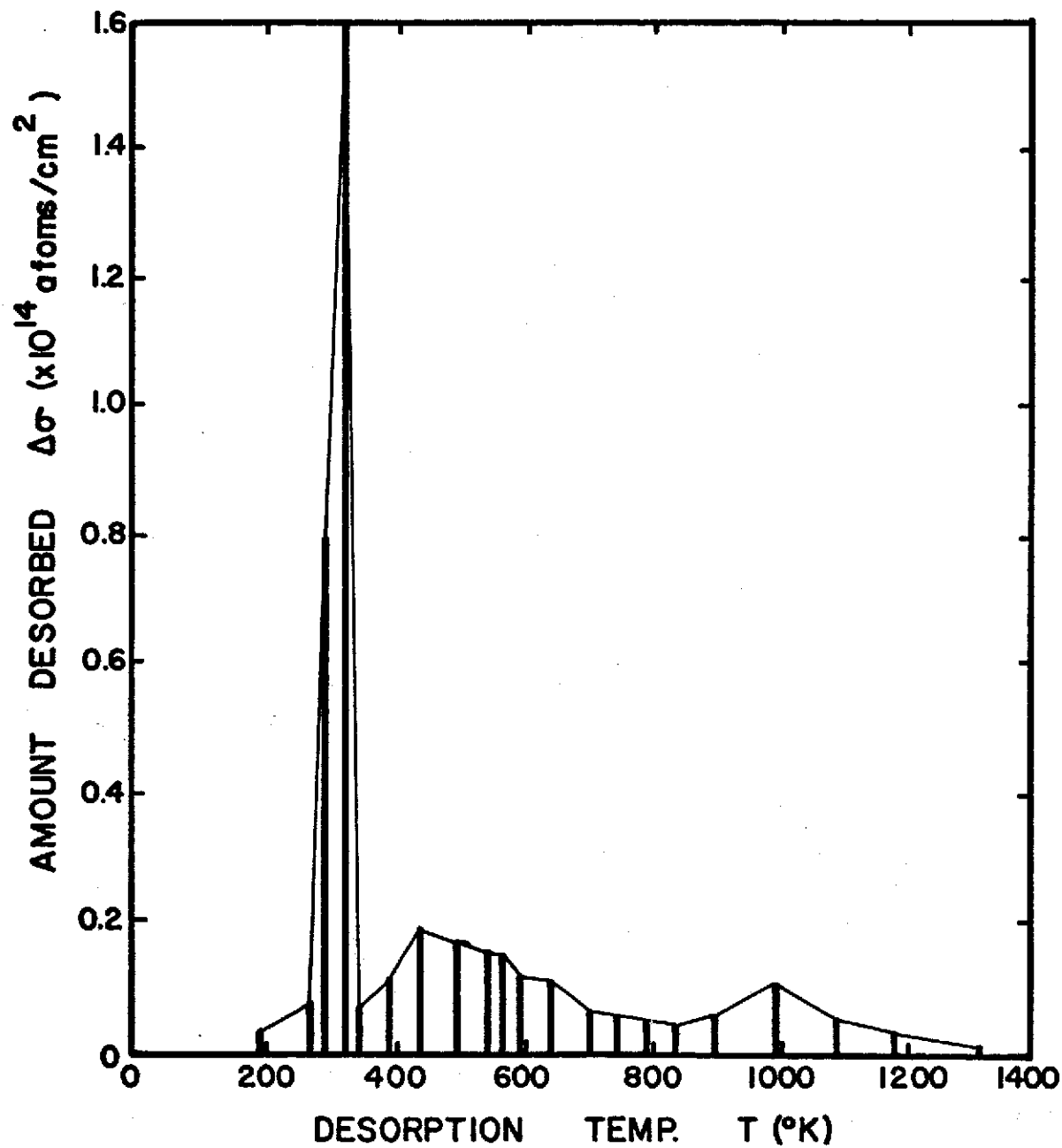


Figure 4

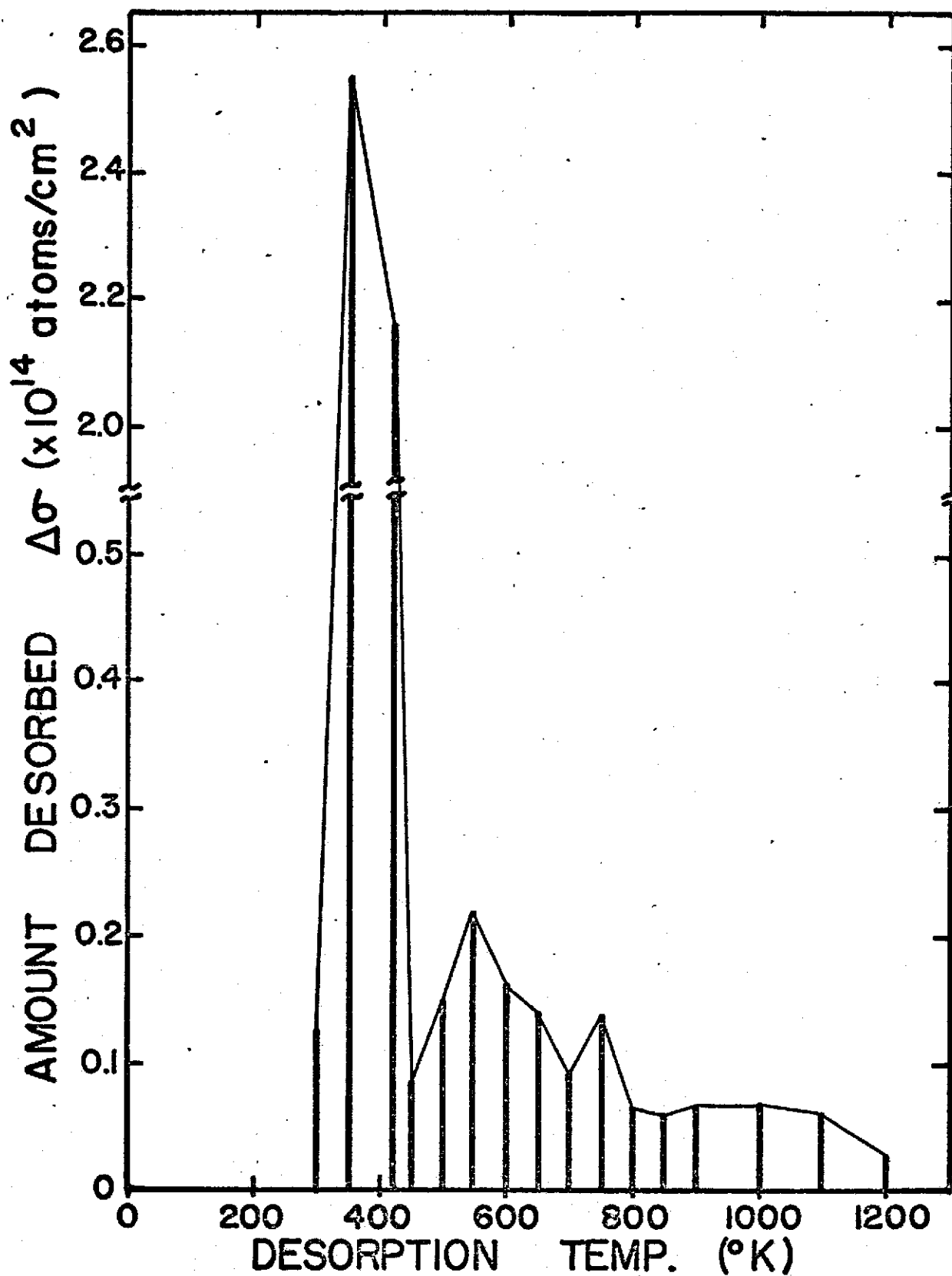
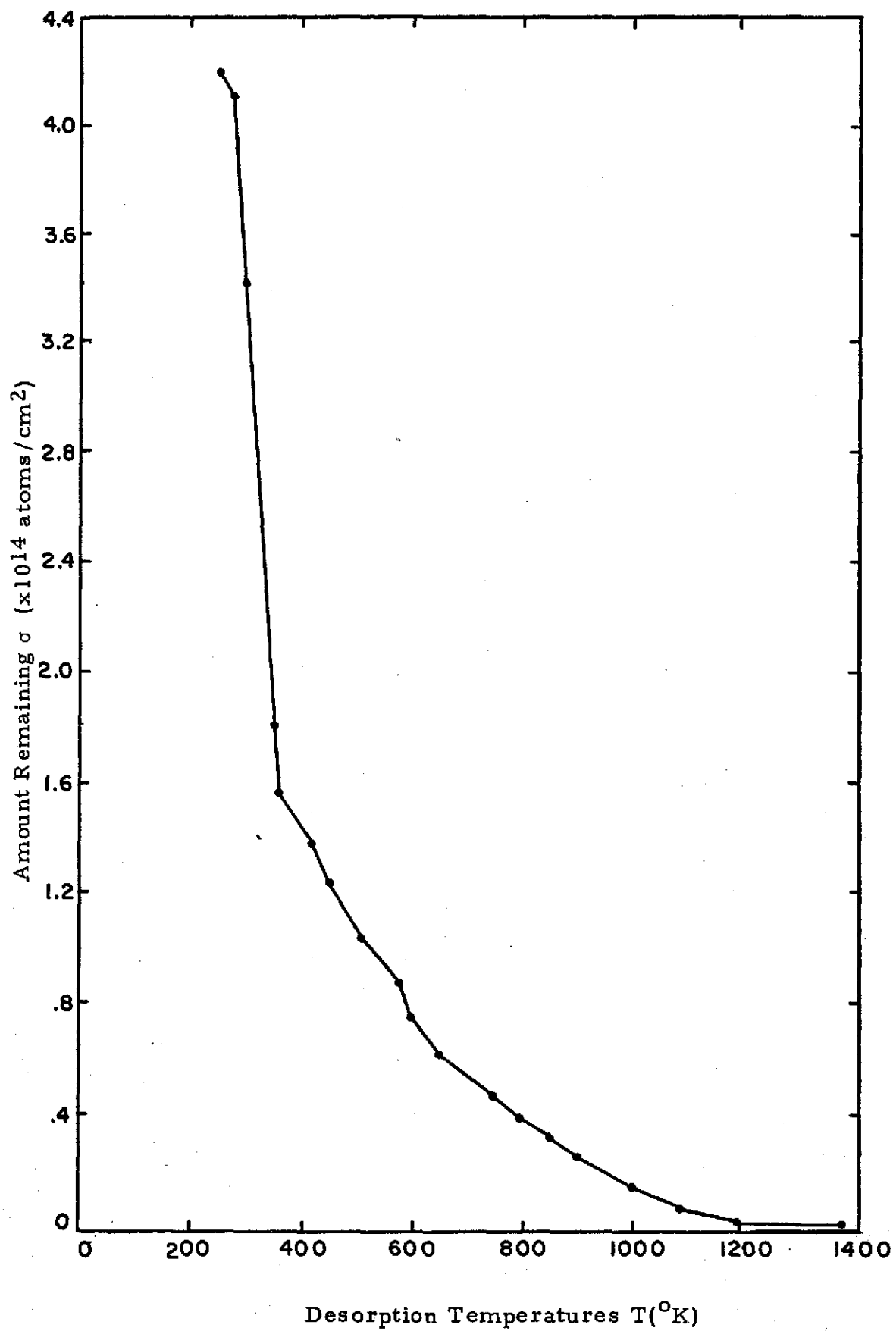


Figure 5



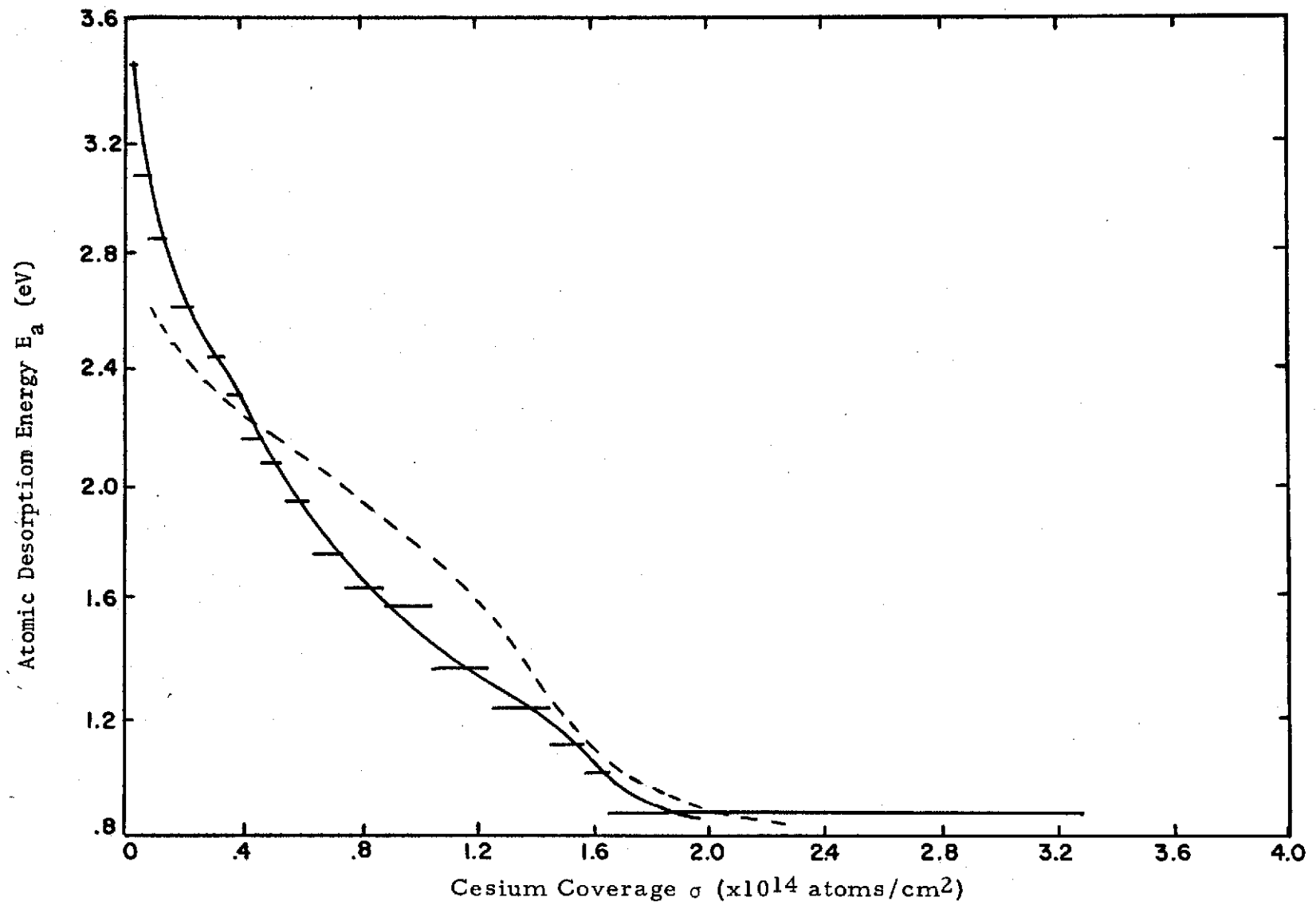
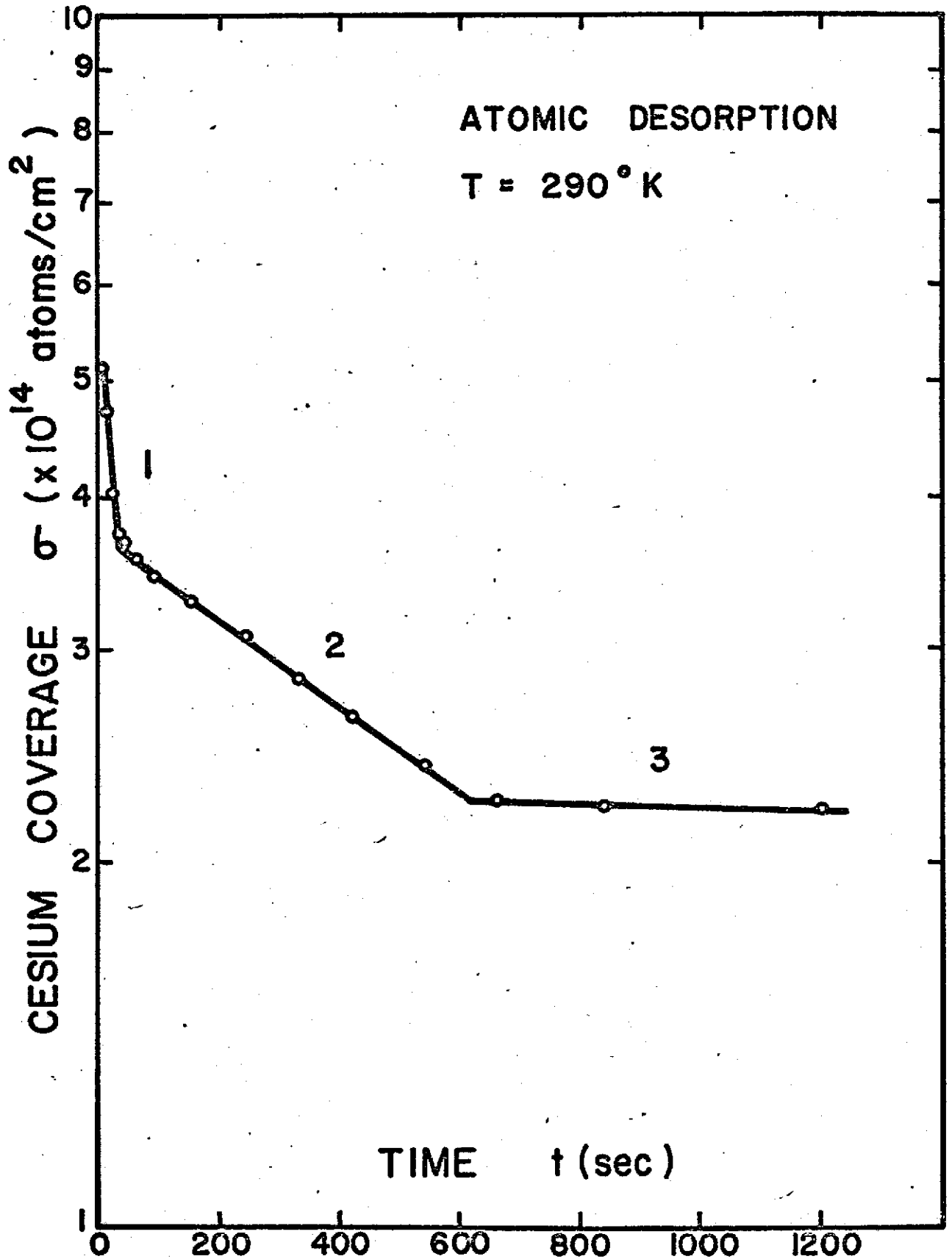


Figure 6

Figure 7



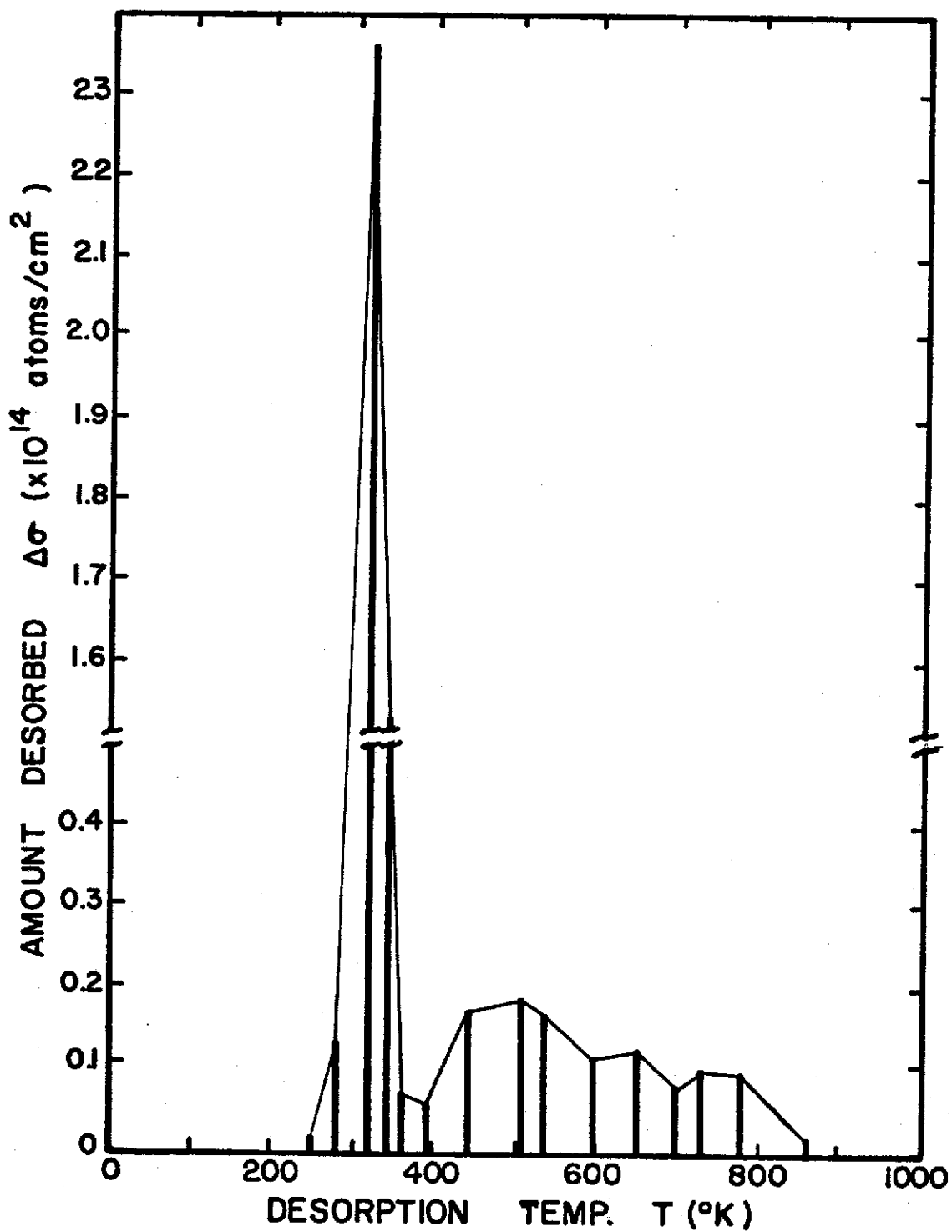
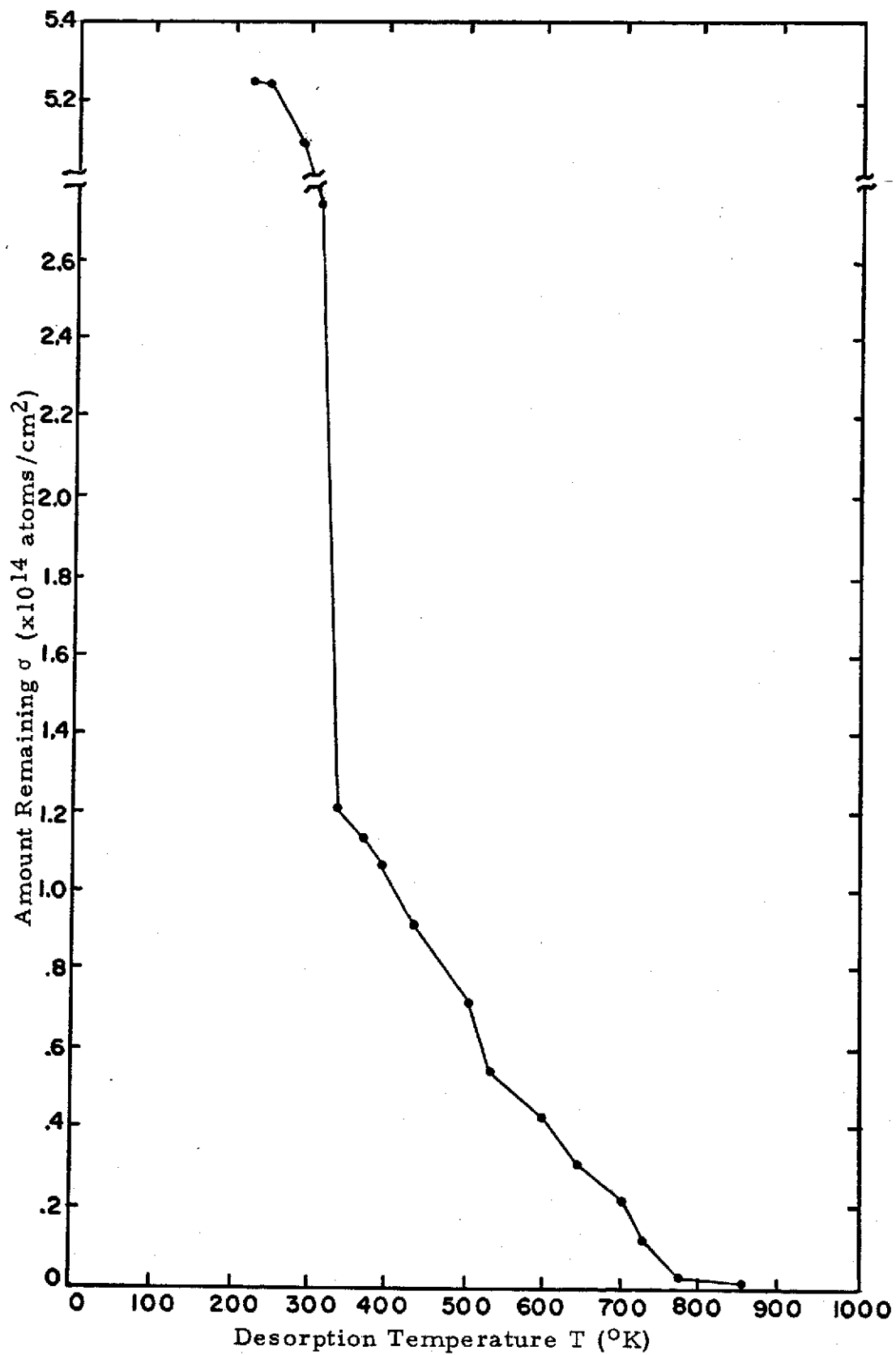


Figure 9



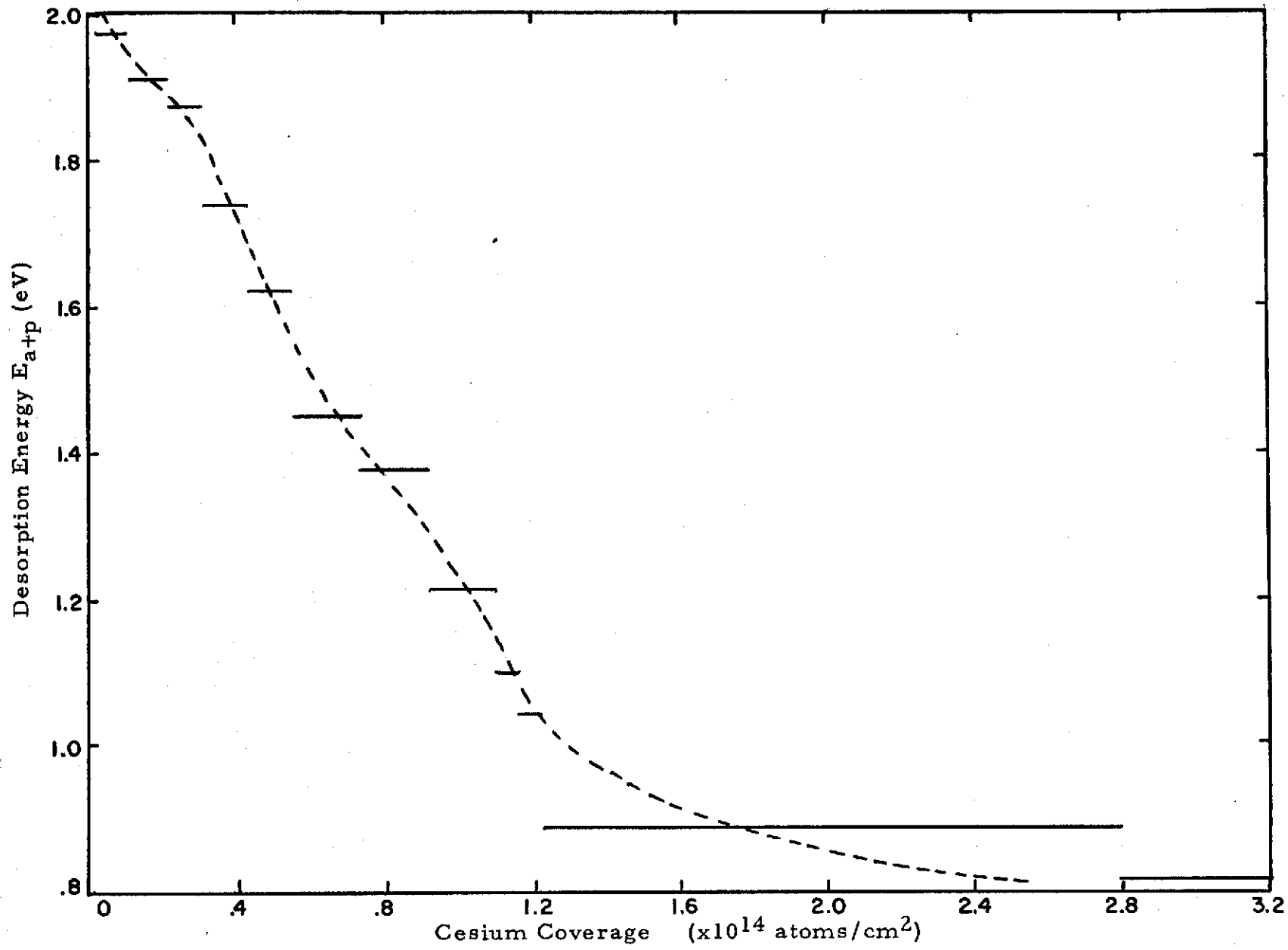


Figure 10

Work Function And Electron Reflection Measurements From The (110) And (100) Planes Of Molybdenum

I. INTRODUCTION

Work function measurements have played a large part in historical investigations of the surface properties of metals; work function changes are a convenient way to monitor the progress and measure the effects of adsorption, both physical and chemical. In addition, clean work function values, which are a useful index of surface cleanliness, recently have been of increased theoretical and practical value. The latter interest arises because of the importance of high and low work function surfaces in electron emission devices of practical interest. The purpose of the experimental program described in this report is to investigate the absolute work function properties of refractory materials suitable for use in thermionic converters.

Early work on work function measurements resulted in disagreement among workers for the following reasons: surfaces were contaminated due either to poor vacuum or to difficult to remove surface contaminants; the orientation of the crystal surfaces were uncertain and finally the reliability of the work function technique chosen was open to question.

Most methods of measuring work function have relied upon measurements of the electron emission properties of the surface of interest.

The emission of electrons has been generated either by adding energy to the electron emitter, as in thermionic and photoelectric methods or by deforming the work function barrier to permit electron tunneling as in field emission. These methods rely on the use of suitable models for describing the electron density of states in the metals investigated. Most early workers assumed the validity of the Sommerfeld free electron model, as a reasonable first approximation. However, most metals are markedly non-free electron-like; Itskovitch¹ has described the effect of this on work function measurements based on thermionic, field and photoelectric processes. In addition experimental field emission studies have confirmed the shortcomings of the Sommerfeld model with respect to results from all the crystallographic directions of tungsten, and molybdenum and copper.^{2, 3, 4}

An absolute method of work function measurement is used in this work which largely overcomes the difficulties discussed above; this method is the field electron retarding potential (FERP) technique. Only one other non-relative method of determining the absolute work function is available – the Shelton⁵ method and this is based again on measurements of the electron emission process so that it, too, is affected by the theoretical problems discussed above. The FERP method, introduced by Henderson⁶ has been neglected except for recent studies of polycrystalline substrates by Holscher⁷ and Kleint.⁸ In the FERP technique the crystal surface is placed as electron

collector while the electron emitter is a field emission tip. The collection of electrons in the FERP method depends only on the height of the collector work function barrier and not on details of the electronic structure of the collector while emission of electrons from the field emission source takes place with its maximum either close to, or at the Fermi level. In the simplest variant of the FERP method, with the emitter close to 0°K, electrons will just be collected when the potential difference between the emitter and collector is ϕ_c , the collector work function value. In this work, correction is made for emitter temperatures above 0°K and for instrumental effects which lead to a perturbation of the emitted electron energy distribution.

In the following section, we describe in detail the theoretical basis for the FERP⁹ method and its experimental application to the measurement of single crystal work functions together with the results from two molybdenum substrates of specified orientation. A useful accompaniment to the work function information generated by the FERP technique is the possibility of accurately measuring elastic and inelastic reflection coefficients for electrons with energies close to zero.

LEED, Laue and Auger techniques in an UHV environment have been used to characterize the surface cleanliness and orientation of the crystals studied.

II. THEORETICAL CONSIDERATIONS

The expression for the differential field emitted current dI_c between energy ϵ and $\epsilon + d\epsilon$ (where $\epsilon = E - E_f$) in the case of a free electron model is given as follows:

$$dI_c/d\epsilon = I_0 e^{\epsilon/d} / \left[(1 + e^{\epsilon/pd}) d \right] \quad (1)$$

where $p = kT/d$ is a dimensionless parameter. The value d is given by

$$d = \sqrt{eF/2(2m\phi_e)^{3/2}} t(y) = 0.976F/\phi_e^{1/2} t(y) \text{ (eV)} \quad (2)$$

where the electric field F and the emitter work function ϕ_e are in $V/\text{\AA}$ and eV, respectively. The maximum emitter current I_0 in Eq. (1) is given by the well known Fowler-Nordheim equation

$$\begin{aligned} I_0 &= \frac{e^3 F^2 A_0}{8\pi h\phi_e^2 t^2(y)} \exp \left[-4(2m\phi_e)^{3/2} v(y)/3\sqrt{eF} \right] \\ &= \frac{1.5 \times 10^{10}}{\phi_e^2 t^2(y)} F^2 A_0 \exp \left[-0.983 \phi_e^{3/2} v(y)/F \right] \text{ (A)} \end{aligned} \quad (3)$$

where A_0 is the area of the emitting surface from which the collected current originates. The image correction terms $t(y)$ and $v(y)$ are slowly varying tabulated functions of the auxiliary variable $y = (e^3 F)^{1/2} / \phi_e$.

From Eq. (1), it is apparent that $dI_c/d\varepsilon$ turns on abruptly at the emitter Fermi level when p is small and decays exponentially with decreasing electron energy. The value of the half width Δ of the TED can be obtained from Eq. (1) so that at $p=0$, Δ is given by

$$\Delta \approx 0.69d. \quad (4)$$

Since the practical value of d varies from 0.1 to 0.3 eV, the experimental half widths fall in the range 0.07 to 0.2 eV.

For the retarding potential method, as diagrammed in Fig. 1, the emitted electrons can be collected at a metal surface of work function ϕ_c only if their total energy E meets the condition

$$E > \phi_c + E_f - V_c$$

where V_c is the emitter-to-collector bias potential; thus, increasing V_c allows all electrons down to the energy level $\varepsilon = \phi_c - V_c$ to be collected at 0°K . The condition $V_c = \phi_c$ represents the current cutoff since electronic states above E_f are not populated, and the total collected current I_c at a specified value of ε is given by

$$I_c = \frac{I_o}{d} \int_0^{-\varepsilon} e^{\varepsilon/d} d\varepsilon = I_o (1 - e^{-\varepsilon/d}). \quad (5)$$

By rewriting Eq. (5) in the working form

$$\log_{10}(I_o - I_c)/I_o = \phi_c/2.3d + V_c/2.3d. \quad (6)$$

This equation, plotted in Fig. 2 at several values of d , may be used to obtain the theoretical value of ϵ_p which is equal to $\phi_c - V_p$. Since V_p (the position of maximum dI_c/dV_c on the energy axis) can be obtained experimentally, the value of ϕ_c can be obtained directly from the TED curve and Fig. 2. Since in practice $\epsilon_p \approx 30\text{mV}$ this method gives ϕ_c easily within 1% accuracy.

Even though the assumptions of the Sommerfeld free electron model, upon which Eq. (1) and the subsequent equations are based have recently been found to be inadequate for certain crystallographic directions of tungsten² and molybdenum³, the occurrence of the emission threshold at E_f was unchanged for clean emitters. In any case, inadequacies in Eq. (1) due to band structure effects can be easily avoided for this application by choosing an emission direction (e.g., the $\langle 111 \rangle$ or $\langle 310 \rangle$ of tungsten) for which the corresponding TED curve agrees well with Eq. (1). For that reason we have utilized for this study oriented field emitters with these directions along the emission axis. Thus, all that must be known concerning the emitter in order to apply the FERP method of work function determination is the value of d which can either be calculated with sufficient accuracy from the $I(V)$ characteristics of the emitter using Eq. (2) or determined experimentally from Eq. (6).

III. ELECTRON REFLECTION

Only one property of the collector that can detract from the complete applicability of the above equations in evaluation of ϕ_c is electron reflection near the threshold of collection which cannot be eliminated by the FERP method should it occur. We can indicate the effect of reflection on Eq. (1) by noting that $I_c = I_p(1-R)$, where I_p is the primary beam current impinging on the collector, and by defining the energy dependent reflection coefficient $R(\epsilon)$ as $R(\epsilon) = I_r/I_p$, where I_r is the reflected current. With these definitions one may readily show that the experimentally measured quantity $dI_c/d\epsilon$ is given by

$$dI_c/d\epsilon = \alpha(\epsilon) dI_p/d\epsilon - I_p d\alpha/d\epsilon \quad (9)$$

where $\alpha(\epsilon)$ is the electron acceptance coefficient and $\epsilon = |\phi_c - V_c|$ is the maximum kinetic energy of the collected electrons. Near the collection current threshold (i. e., $\epsilon \sim 0$) the last term of Eq. (9) will be small compared to the first since $I_p \rightarrow 0$ as $\epsilon \rightarrow 0$ and $d\alpha/d\epsilon$ is normally small at $\epsilon = 0$.

However, as the energy of the primary electron beam increases above the threshold voltage considerable change may occur in $\alpha(\epsilon)$ (i. e., $d\alpha/d\epsilon$ becomes large) which in turn will cause serious deviation in the apparent value of I_p . Thus, plotting the data according to Eq. (6) in order to obtain an accurate value of ϕ_c and d will not be possible. In

like manner it will be difficult to utilize Eq. (7) in order to obtain ϕ_c due to the inability to obtain an accurate value of I_o .

In contrast, Eq. (8) is basically unaffected by reflection since the last term of Eq. (9) can usually be neglected at $\epsilon \approx \epsilon_p$. We should also point out that a cursory examination of Fig. 2 reveals that ϵ_p is very small (less than 40 mV) at practical values of d and T so that uncertainties in the exact position of ϵ_p due to reflection will not introduce appreciable error in the value of ϕ_c . Thus, in the event that detectable reflection should occur for a particular collector at threshold the evaluation of ϕ_c should be accomplished from the TED curve through Eq. (8).

IV. EXPERIMENTAL

Crystal Preparation: Polishing, Mounting and Laue Patterns.

A (100) and a (110) orientation Mo crystal were cut from single crystals of Mo into discs about 300 mil diameter and 50 mil thick. One side of each was ground and then polished using alumina polishing grit, initially 800 mesh, finally 5μ diameter. Next Laue patterns were obtained in order to check the orientation of the disc material. If this was more than 3° from the required orientation, the crystals were reground and polished. The shift, $2x$, of the Laue pattern center as the crystal is rotated through 180° provides a measure of the inclination of the crystal surface, θ , with the planes of interest; θ is obtained from $\tan 2\theta = x/d$ where d is the distance from the

film to the crystal surface, adjusted in the present case to 1".

Each Mo disc was enclosed in a small tight fitting Mo ring of the same thickness as the single crystal disc. A light spot weld sufficed to secure the disc to the ring which was in turn spot welded more heavily to a 20 mil supporting lead of Mo. Behind each polished face of the supported crystals a 10 mil heatable W hairpin filament was placed as a thermionic source for electron bombardment of the crystal.

Crystal Cleaning: LEED Auger Techniques.

Heat treatment to $\sim 2000\text{K}$ was the primary technique used to clean the crystals except when significant carbon was detected in which case the oxygen etch treatment was used. This involved prior treatment of the ion pump by subjecting it to several cycles of Ar instability treatment before the oxygen was introduced to the crystal. Musket and Ferrante¹¹ have pointed out that the Ar treatment is necessary in order to reduce the CO/O_2 ratio below 1% for an O_2 pressure of 5×10^{-8} torr. The oxygen etch treatment involved heating the crystal in the presence of $\approx 10^{-7}$ torr of oxygen. After pumping away the O_2 , the crystal was flash heated to $\sim 2000\text{K}$ to remove the surface oxide.

The LEED information was obtained in a 4 Grid Varian display system which also served to gather the Auger information which was generated by bombarding the crystal at normal incidence with a 10-20 μA , 1500V/electron

beam. The two middle grids were connected together and modulated with a 5 volt p-p ac signal superimposed on top of a variable (0-1500V) negative dc voltage V_g generated by a Kepco F.G. 100 function generator and a 0-1500V Kepco programmable dc supply; V_g prevented electrons of energy less than V_g from reaching the collector. Auger currents were detected by using a PAR HR-8 lock-in voltmeter to measure the voltage developed across a suitable load. The lock-in voltmeter was tuned to the second harmonic of the grid modulating signal so that the output was proportional to the second differential (d^2I_c/dV_g^2) of the collected current with respect to the grid voltage V_g ; the quantity d^2I_c/dV_g^2 is proportional to the Auger current and is widely used as a measure of it. Two kinds of load circuits were used: a 300k Ω resistor, in which case the modulating frequency applied to the grids was kept below $\sim 300H_z$ in order to avoid capacitive loss of signal; and a parallel RC circuit tuned to 3400H $_z$ in which case the modulating frequency was 1700H $_z$. The LC circuit consisted of a 2 henry, high quality, inductor L (UTC. FO2) in parallel with a capacitor C. At resonance the circuit presents a high impedance load to the second harmonic signal of interest, a considerably diminished load to the interfering 1st harmonic signal and a very low load ($\sim 70 \Omega$) to the dc component of the collector current. Two advantages of the LC circuit compared to the resistive load are that stray capacity in the collecting cables etc. merely add to the capacity of the LC

circuit where they produce a slight shift in resonance frequency. In the resistive load situation, stray capacitance serves to diminish the output voltage signal by providing a low impedance shunt to ground. The second advantage of the LC load is the possibility of operation at higher frequencies where the $1/f$ noise is considerably smaller. This is not possible for the resistive load since the impedance of the stray capacitance path diminishes as f increases.

Work Function, Reflection Measurements.

These measurements were performed with the aid of a FERP gun described in earlier reports in this series.⁹ A sketch of it is shown in Fig. 3. The cathode consists of a W field electron emitter; this is followed by two Einzel electron lens L1 and L2 to produce a parallel beam of electrons of variable energy in the range 0-150V. These impinge normal to the crystal of interest after passing through a mesh just in front of the crystal. Since field emitted electrons originate from the emitter Fermi level they will just begin to be collected only if the collector voltage V_c is positive with respect to the emitter by an amount $V_c \geq \phi_c$, where ϕ_c is the collector work function. Hence, measurement of the onset voltage, V_c , provided a measure of ϕ_c . Three parameters affect performance of the FERP gun: the voltage of Einzel lens L1, the voltage of Einzel lens L2 and the mesh potential. Of these the lens elements voltages are the most important. Two operating modes were used, in the first, the potentials of L1 and L2 were adjusted to

produce maximum transmission. This mode was used in reflection measurements. In the second mode, the potentials were adjusted to produce best resolution. This mode was used in work function measurements and was determined by varying V_{L1} , V_{L2} to produce the smallest differences between the 10 and 90% points¹² in the leading edge of the field emission TED plots. The onset method of obtaining work function, which was described above, was not used to determine ϕ_c ; rather the position of the TED peak was used instead as described in Section II. The TED plots represent the differential of I_c with respect to V_c at constant mesh potential; dI_c/dV_c was measured directly by modulating the field emitter with a 25-50 mv p-p ac voltage and monitoring the voltage developed across a suitable load while the load was swept through a 0-6v range provided by the Kepco FG function generator. The load choice was the same as that available for the Auger measurements described in Section II and the load potential was also measured with a PAR HR-8 lock-in amplifier. For the work function measurements, the HR-8 was tuned to the 1st harmonic of the emitter modulating voltage in order to obtain dI_c/dV_c . This was plotted on a X-Y recorder as a function of V_c . In order to accurately measure the position of the peaks of the plot of dI_c/dV_c , a Keithly digital voltmeter (model 241) was used to place accurate vertical marks on the X-Y plot in the vicinity of the TED peaks.

With the FERP electron gun operated in its mode of maximum transmission, the crystal was bombarded with a 10^{-8} - 10^{-7} amp electron beam during which the collector current was measured as a function of collector voltage for fixed values of the FERP gun mesh potential. The mesh, which is part of the last gun electrode, is about 1/3 of a crystal diameter in front of the crystal and was maintained either close to the cut-off potential (6-10v) or considerably higher at 150V. The FERP gun will only deliver electrons if the mesh potential, V_m , satisfies $V_m \geq \phi_{\text{mesh}}$ where ϕ_{mesh} is the mesh work function. In the present case $\phi_m \sim 5.3$ eV so that mesh potentials greater than ~ 6.0 eV should be sufficient to prevent any field emitted electrons from being cut-off. When the mesh was operated close to cut-off, only elastically reflected electrons escaped from the crystal as the crystal potential was swept through the range of interest -- 0-30V or 0-150V; on the other hand mesh potentials of 150V permitted escape of inelastically scattered electrons as well.

V. EXPERIMENTAL RESULTS

Laue Results

The 0° and 180° Laue patterns for Mo(100) and for Mo(110) indicate that the crystal surfaces were aligned to within 1.1° of the intended direction for the (110) crystal and within 2.2° for the (100) oriented crystal.

LEED Results

LEED patterns of Mo(110) are shown in Figs. 4 both before (4a) and after (4b) work function measurements were obtained. Together with the Auger data, these patterns clearly indicate contamination by carbon. Although an initial attempt to remove carbon by the oxygen etch method discussed in Section II, was unsuccessful, a final attempt after the work function/reflection data had been obtained was successful. After the final argon change was pumped away, an oxygen etch of the crystal was carried out by heating the crystal for 20 hours at $\sim 1800^{\circ}\text{K}$ in the presence of $\sim 10^{-7}$ torr of oxygen. At the completion of the etching and pumping away of the oxygen, the crystal was flash heated to $> 2000^{\circ}\text{K}$. A LEED pattern taken at this point (Fig. 4c) is representative of a clean (110)W surface.

Because both the LEED pattern and Auger information again indicated the presence of carbon of the flash heated Mo(100) crystal, the oxygen etch treatment described above was also carried out for the 100 crystal. In this case the etch treatment was successful at first try; the resulting LEED patterns of the clean flash heated crystal are shown in Fig. 5 and are indicative of the clean (100) surface of Mo.

Auger Results

The (110) crystal behaved in an interesting fashion: after flash heating to $\sim 2000^{\circ}\text{K}$, the "cleaned" crystal produced an Auger (Fig. 6A) pattern

containing a large peak at $\sim 145\text{V}$ which was attributed to S for which the main peak should fall at 148V . Further heating of the crystal diminished the S peak and increased the small C peak (266V) and after extensive flashing to $T > 2000^\circ\text{K}$ the carbon peak grew in intensity as flashing proceeded while the S diminished (See Fig.6B). The final ratios (see Fig. 7) of the S and C peaks to the largest peak ($1/2$ of the peak to peak value was used - the middle of the peak being at 195V) were ~ 0.04 and 0.30 respectively. Some evidence of small amounts of other impurities were also noticed occasionally. Mostly this was O presumably as part of CO molecules since the O peak diminished along with the C peak as a result of heating the crystal. The remaining C peak was felt to be due to the presence of surface carbon not bound up as CO.

The (100) crystal was also contaminated with carbon (see peaks at 270V) which increased during the initial flashing procedure (Fig. 8). However, the initial oxygen etch treatment was successful as evidenced by the Auger plots in Fig. 9 obtained after oxygen etch treatment. Fig 10B was obtained after a quick heat of the crystal when the vacuum was good enough to ensure no recontamination by adsorbed residual gas. Notice the absence of C and O whereas Fig. 10A obtained after allowing the crystal to sit for a while in the presence of residual gas indicated a gradual build up of adsorbed CO present as indicated of the increased C peak at 270V and the larger oxygen peak at 500V .

Vacuum Environment for Work Function and Electron Reflection Measurements.

It was not found possible to operate the FERP gun in the LEED vacuum chamber either because, when mounted in the horizontal position, the earth's magnetic field interfered or because of inadequate vacuum conditions. For this reason, at the completion of the LEED - Auger measurements the FERP gun/crystal was transferred to a different vacuum system allowing improved vacuum environment capable of $\sim 10^{-10}$ torr vacuum and one in which the FERP gun was mounted vertically. In this location the earth's magnetic field is close to the vertical so that interference from the earth's magnetic field is minimal.

Work Function Results

The work function results are displayed in Table I along with results by other workers who used different techniques than the one used here.

The Mo(100) plane results indicate that $\phi = 4.183 \pm 0.017$ eV, while the Mo(110) plane yielded a $\phi = 4.920 \pm 0.050$ eV. The (110) plane value was for a slightly, carbon contaminated plane.

Electron Reflection Results

Electron reflection results were obtained in two energy ranges 0-25V and 0-140V and in two modes - elastic mode in which the mesh potential

was kept low in range (7-10)V so that mostly elastically reflected electrons, only, were returned to the mesh - and a mode in which the mesh was maintained at +150V so that both elastic and inelastically reflected electrons were returned to the mesh.

Reflection coefficients were calculated on the basis of the following analysis. A fraction T of the current I_p arriving at the mesh from the emitter is transmitted so that TI_p is the current arriving at the collector crystal. A fraction $(1-R)$ of this is collected where T is the collector reflection coefficient so that the collector current I_c is given by

$$I_c = I_p T(1-R) \quad (10)$$

If we assume that all reflected electrons are collected by the mesh I_m then the total current I_t collected by the mesh and collector combined is given by

$$I_t = I_c + I_m = I_p, \quad (11)$$

so that the ratio $r = I_c / I_t$ is given by

$$r = T(1-R). \quad (12)$$

Hence, $R = 1-r/T$ so that R may be determined by measuring the ratio $r = I_c / (I_m + I_c)$ at each value of collector potential. This method of calculating R automatically compensates for a drop off in I_p due to emitter

contamination. The value of T was taken to be 0.64 based on optical inspection.

At low values of V_g , correction was made for the drop in collected current due to the energy spread of the field emission beam.

The results for the Mo(110) and Mo(100) crystals are displayed in Figs. 11-15. Two sets of curves were obtained for the (100) crystal: the first, Fig. 11, refers to a slightly contaminated crystal in which the crystal was still covered with a partial monolayer either of CO or of oxide. At this point the work function of the crystal was about 4.72eV which corresponds to a work function increment of 0.5eV over that of the clean surface. The second set (Figs. 12, 13) of Mo(100) reflection curves was obtained after the Mo(100) crystal had been cleaned by flash heating. Figures 14 and 15 were for the slightly carbon contaminated Mo(110) crystal.

VI. DISCUSSION

Work Function Values

Few calculated results of absolute work function values are available for comparison with experiments and these are concerned for the most part with average estimates and provide no information about specific planes. Two studies are available however, which compute individual plane work functions: an earlier work by Smoluchowski¹² concerned with W work functions and a more recent semi-empirical study by Gyftopoulos and Steiner¹³

which permits calculation of work functions for a wide variety of substrates of any surface orientation. Calculations have been carried out for Mo leading to predicted values of 5.23eV for Mo(110) and 4.44eV for Mo(100). These values are both somewhat higher than the values obtained in this work. However, the difference between the calculated values (0.79eV) is quite close to the difference between the experimental values (0.73) measured here; of more concern is the apparent discrepancy between the Mo(100) work function value determined in this work (4.18eV) and the higher values (~ 4.35 eV) obtained by other workers. However, since the present sample cleanliness was carefully monitored by the Auger technique, and because the FERP method is felt to be the most reliable, the present value would seem to be the most trustworthy.

Surface Impurity Concentration Estimates

Without performing calibration experiments, a crude estimate of carbon surface concentration N^C may be obtained by using the approach of Bishop and Rivière¹⁴ who derived the following expression for the Auger electron current due to the presence of an element present at the surface of another material.

$$I_{\text{Auger}} = I_0 N \left(\frac{\Omega}{4\pi} \right) \cos(\text{cosec } \phi) \phi(U) \quad (13)$$

Where I_0 is the incident primary electron beam current, Ω is the solid

angle subtended by the collector, s is the correction for additional ionization due to back-scattered electrons, ϕ is the angle of incidence of the primary beam and $\sigma(U)$ is the cross-section for ionization of an inner atomic level which, in the case of C, is in the K shell and in the case of Mo is in the M shell. Although r varies from one element to another its variation is small and we neglect it here i.e., we assume $s = 1$ for both Mo and C. Since I_0 and ϕ are the same for different elements on the same surface we have

$$\frac{I_{\text{Auger}}^{\text{Mo}}}{I_{\text{Auger}}^{\text{C}}} = \frac{\phi^{\text{Mo}}(U) \cdot N^{\text{Mo}}}{\phi^{\text{C}}(U) \cdot N^{\text{C}}} \quad (14)$$

where N^{Mo} and N^{C} are the surface concentrations of Mo and C respectively and where $\phi(U) = (b/E_c^2) f(U)$ in which E_c is the critical ionization potential of ionized shell electrons; $U = E_p/E_c - E_p$ being the primary beam energy and $f(U)$ a function of U . For Mo and C we take respectively E_c to be $\sim 190\text{V}$ and 270V . Using a value of $E_p = 1500\text{V}$, the corresponding values of U for C and Mo are 5.6 and 7.5 respectively. From a plot of $f(U)$ vs. U given in Bishop and Riviere's work we find that $f(U) = 0.45$ for C and 0.39 for Mo. Values of b given in Bishop and Riviere's work are 0.35 for K electrons and 0.25 for L shell electrons. Presumably the M shell value is lower still and we shall use a value of 0.15 for this shell - inner shell ionization in Mo taking place from the M shell. Hence,

$$\begin{aligned} \phi^{\text{Mo}} / \phi^{\text{C}} &= (b^{\text{Mo}} / b^{\text{C}}) (E_{\text{c}}^{\text{C}} / E_{\text{c}}^{\text{Mo}})^2 (f^{\text{Mo}}(\text{U}) / f^{\text{C}}(\text{U})) \\ &= (0.15/0.35) (270/190)^2 (0.39/0.45). \end{aligned} \quad (15)$$

Hence, $\phi^{\text{Mo}} / \phi^{\text{C}} \sim 0.75$. Equation (14) may now be used to estimate $N^{\text{C}} / N^{\text{Mo}}$ provided $I^{\text{C}} / I^{\text{Mo}}$ is known. The Auger current due to Mo is split up among several peaks and will be assumed to be proportional to the sum of the heights of all of them. In this case from Fig. 7 we estimate $I^{\text{C}} / I^{\text{Mo}} \sim 0.06$ so that $N^{\text{C}} / N^{\text{Mo}} \sim 0.045$. Hence, carbon contamination of the Mo(110) crystal was about 5% of a monolayer. Clearly this is a very rough estimate in view of the various assumptions on which the calculation was made.

Reflection Coefficients

An examination of the 0-140V reflection coefficient curves indicates a similar behavior for all three. Thus, the elastic coefficient rises to a maximum in the range 0-10V and then declines steadily with increasing electron energy. The inelastically reflected electrons on the other hand steadily rise from a threshold in the range 0-10V to surprisingly high values at 140V. The most noticeable difference between the clean and contaminated Mo(100) surface is the obliteration of the 0-10V peak in the contaminated curve. Also the threshold for the contaminated curve inelastic reflection coefficient occurs 3-5V lower. In addition the contaminated crystal has a lower elastic coefficient throughout the 0-150V energy range. Interestingly the inelastic

curves for the clean and contaminated crystal are very similar to each other except for the above noted difference in thresholds.

A comparison of the Mo(100) and Mo(110) curves indicates a similar threshold value for the inelastic coefficients and a similar behavior up to 20V, beyond which, however, the (110) plane coefficient remains below the (100) plane value until at 140V, the (110) plane value is only 60% of the (100) plane value.

It is interesting to compare the reflection data obtained here with reflection coefficients found by Khan¹⁶ et. al., and by Swanson⁹ et. al., for W(100) and W(110) since Mo and W are adjacent transition metals in Group VI of the periodic table and both have the same lattice constant. The Mo(100) elastic data presented here is similar in form with the data of Khan et. al., for W(100) in that a broad maximum is presented at $\sim 8V$ together with a smaller shoulder at $\sim 11V$. Also similar is the decline at higher energies although the Mo(100) reflection coefficient does not decline to the low value ($R \sim 0.05$) obtained by Khan et. al., thus for the Mo(100) crystal R is still greater than 0.1 even at 140V. Conspicuously absent in the Mo(100) curve is the low energy peak present both in the data of Swanson et. al., and in the work of Khan et. al. The Mo(110) elastic reflection data exhibits a prominent peak in the R curve at 5V as do the curves of Khan¹⁶ et. al., and Swanson⁹ et. al. Also present in the Mo curve is a plateau which terminates beyond 15V. There are no features present in the Khan work at 15V; however, the R curve of

Swanson et. al., has a pronounced peak at 14V. The most significant difference between the Mo(110) and W(110) work is the high elastic reflection coefficient (0.2) for Mo(110) even at 140V.

In conclusion, we may note that the elastic reflection coefficients are surprisingly similar although the high energy values of R appear to be noticeably higher for Mo than for W.

TABLE I

PLANE	WORK FUNCTION (eV)	TECHNIQUE
Mo (100)	4.18 \pm 0.02	This work
	4.35 \pm 0.02	Field Emission ¹⁷ Fowler Nordheim
	4.35 \pm 0.07	Thermionic ¹⁸
Mo (110)	4.92 \pm 0.05	This work*
	4.81 \pm 0.09	Field Emission- ¹⁷ Fowler Nordheim.
	5.12 \pm 0.16	Combined field emission Fowler Nordheim and Field Emission TED ¹⁷
	5.10 \pm 0.05	Thermionic ¹⁹
	4.90 \pm 0.07	Thermionic ¹⁸
		* For a slightly carbon contaminated surface.

VII. REFERENCES

1. F. I. Itskovich, Soviet Physics JETP 23, 945, 1425 (1966); 24, 202 (1967).
2. L. W. Swanson and L. C. Crouser, Phys. Rev. 163, 662 (1967).
3. L. W. Swanson and L. C. Crouser, Phys. Rev. Letters 19, 1179 (1967).
4. R. D. Whitcutt and B. H. Blott, Phys. Rev. Letters 23, 639 (1969).
5. H. Shelton, Phys. Rev. 107, 1553 (1957).
6. J. E. Henderson and R. E. Badgley, Phys. Rev. 38, 590 (1931).
7. A. A. Holscher, Surface Sci. 4, 89 (1966).
8. C. Kleint, Exp. Tech. Phys. 16, 125 (1968).
9. R. W. Strayer, W. Mackie and L. W. Swanson, Surface Sci. 34, 225 (1973).
10. R. H. Good and E. W. Muller, Handbuch der Physik, edited by S. Flugge (Springer-Verlag, Berlin, 1956), Vol. 21, p. 176.
11. R. G. Musket and J. Ferrante, NASA Technical Note NASA TN D-6399, NASA, Washington, D.C., August 1971.
12. R. Smoluchowski, Phys. Rev. 60, 661 (1941).
13. D. Steiner and E. P. Gyftopoulos, 27th Ann. Conf. on Phys. Electronics.
14. H. E. Bishop and J. C. Riviere, J. App. Phys., 40, 1740 (1969).
15. C. R. Worthington and S.G. Tomlin, Proc. Phys. Soc. A69, 401 (1956).
16. I. H. Khan, J. P. Hobson and R. A. Armstrong, Phys. Rev. 129, 1513 (1963).

17. L. W. Swanson et. al., Investigations of Electron Emission Characteristics of Low Work Function Surfaces, Final Report Contract NASW - 1516 Field Emission Corp., McMinnville, (1967).
18. E. M. Savitskin, et. al., Sov. Phys. - Technical Physics, 11, 974 (1967)
19. U. V. Azizov, et. al., Sov. Phys. Sol. State 7, 2232 (1966).

VIII. FIGURE TITLES

- Fig. 1. Potential energy diagram for a field electron retarding potential analyzer. When the collector is biased such that only electrons from the Fermi level of the emitter can reach the collector, the battery voltage V_c is equal to the collector work function ϕ_c .
- Fig. 2. The difference ϵ_p in energy between the peak of the TED curve and the Fermi level as a function of T and energy parameter d .
- Fig. 3. Diagram of FERP tube showing pertinent features of the electron optical system and collector single crystal.
- Fig. 4a. Initial LEED pattern of Mo(110) after brief flashing of crystal to 1800K. Beam voltage 300V.
- Fig. 4b. LEED pattern after further heating of Mo(110) crystal to $\sim 2000K$. Beam voltage 200V.
- Fig. 4c. Final LEED pattern taken at 140V after Mo(110) crystal had been subjected to oxygen etch and replaced in LEED system and heated to $\sim 2000K$.
- Fig. 5. LEED pattern at 120V of Mo(100) crystal which has been oxygen treated at 10^{-7} torr for 20 hours at 1800K; crystal was then cleaned by flashing to 2000K at $p \sim 2 \times 10^{-9}$ torr.
- Fig. 6. A is an Auger spectrum of a S contaminated Mo(110) crystal while B is an Auger spectrum taken after flash heating of the crystal. Beam current is $\sim 15\mu$ A and beam voltage is 1500V.
- Fig. 7. Auger spectrum of Mo(110) crystal after further heating. Notice the increase in the relative height of the C peak at 270V.
- Fig. 8. Auger spectrum of Mo(100) after flashing. Notice the large C peak. Same operating current etc. as in Fig. 6.
- Fig. 9. Auger spectrum of Mo(100) after oxygen etch treatment. Notice residual C peak at 270V and the residual O peak at 500V.

- Fig. 10. Auger spectrum of Mo(100) after flashing in good vacuum (B) and after allowing to sit for awhile(A). Notice the growth of the C and O peaks in (A) presumably due to adsorption of CO from the gas phase.
- Fig. 11. Electron reflection curves for elastic and inelastically reflected electrons from contaminated Mo(100).
- Fig. 12. Electron reflection curves for elastic and inelastically reflected from contaminated Mo(100).
- Fig. 13. Electron reflection curves for elastic and inelastically reflected electrons from clean Mo(100).
- Fig. 14. Electron reflection curves for elastic and inelastically reflected electrons from clean Mo(110).
- Fig. 15. Electron reflection curves for elastic and inelastically reflected electron from clean Mo(110).

Figure 1

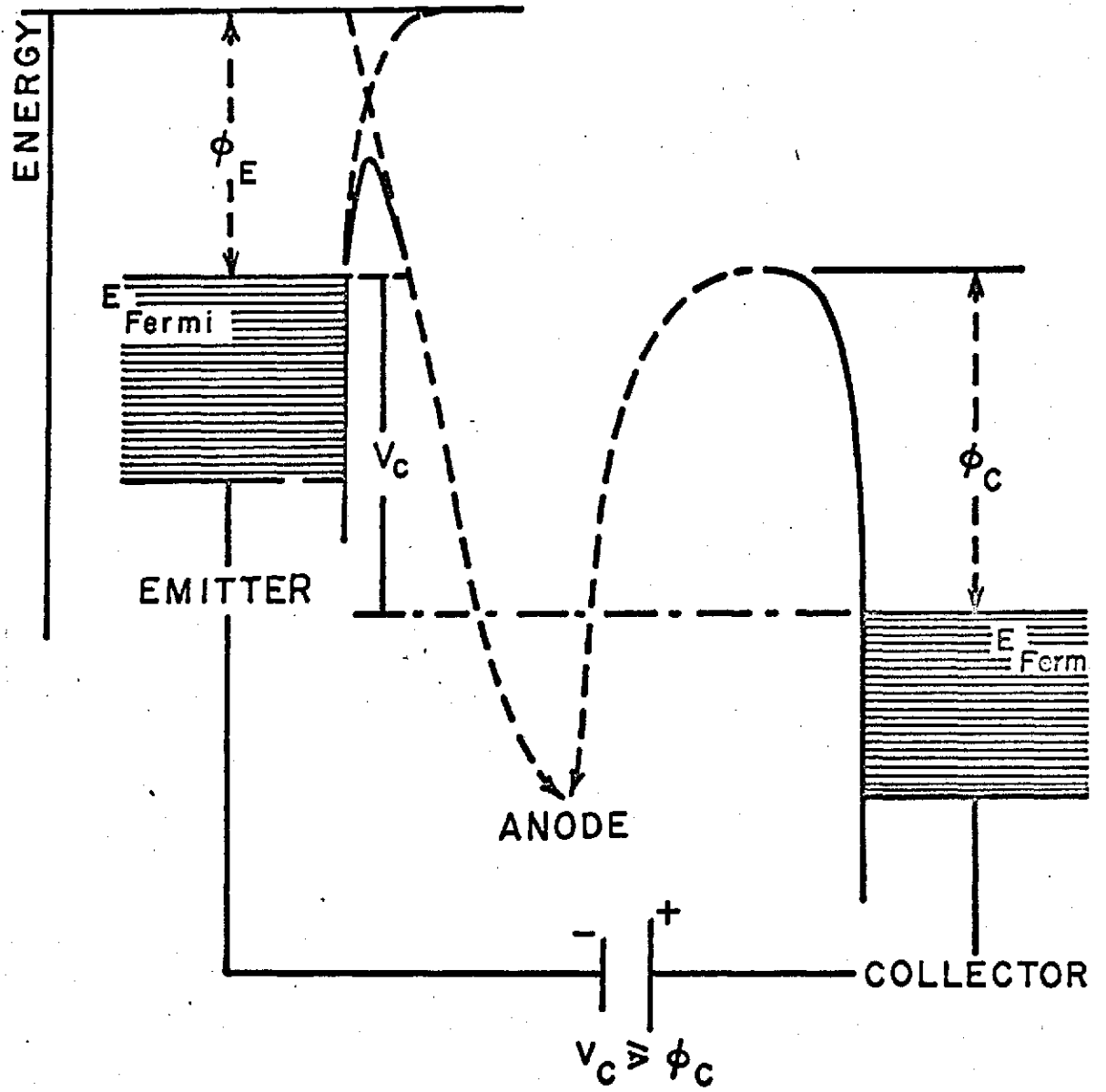
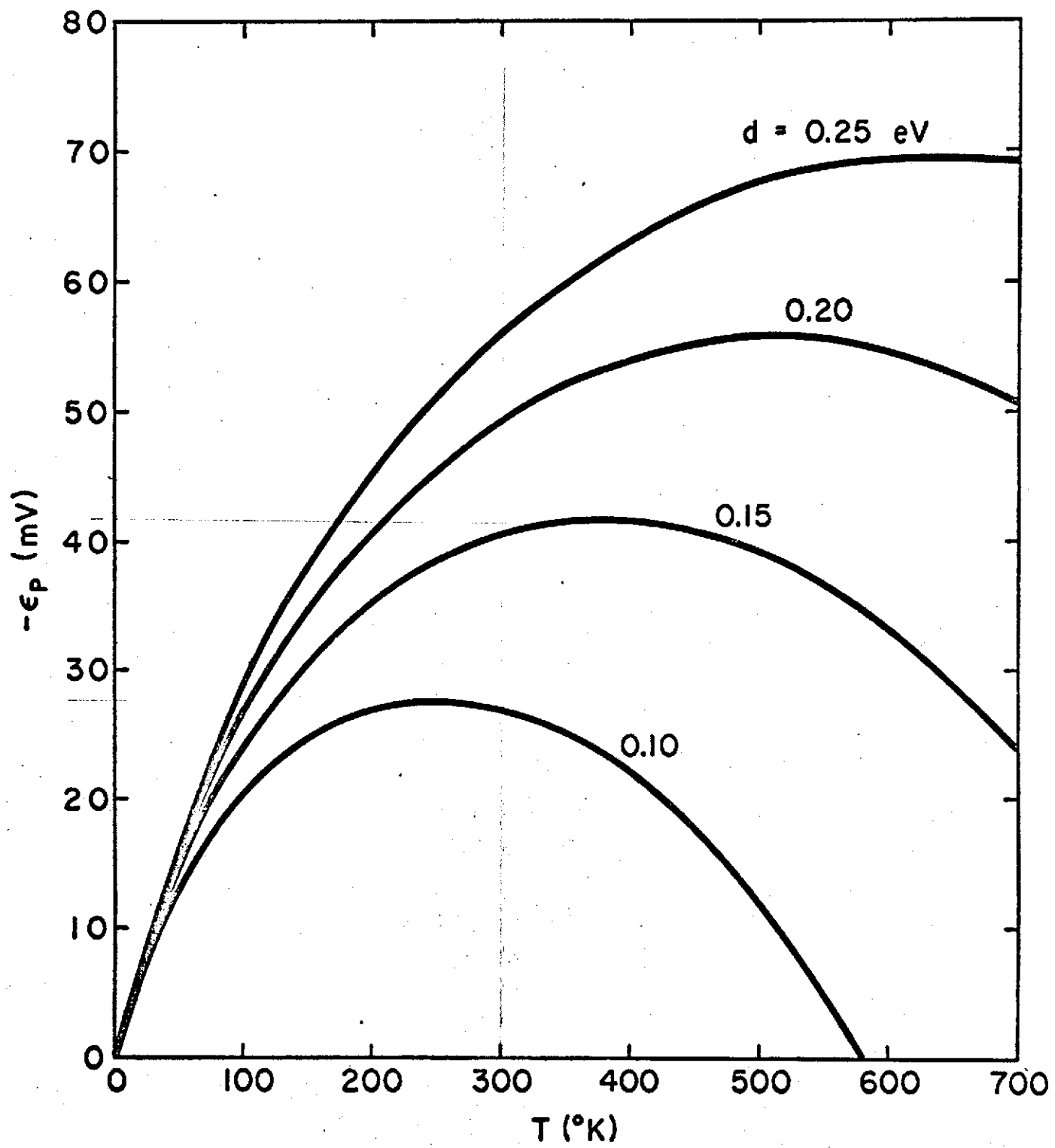


Figure 2



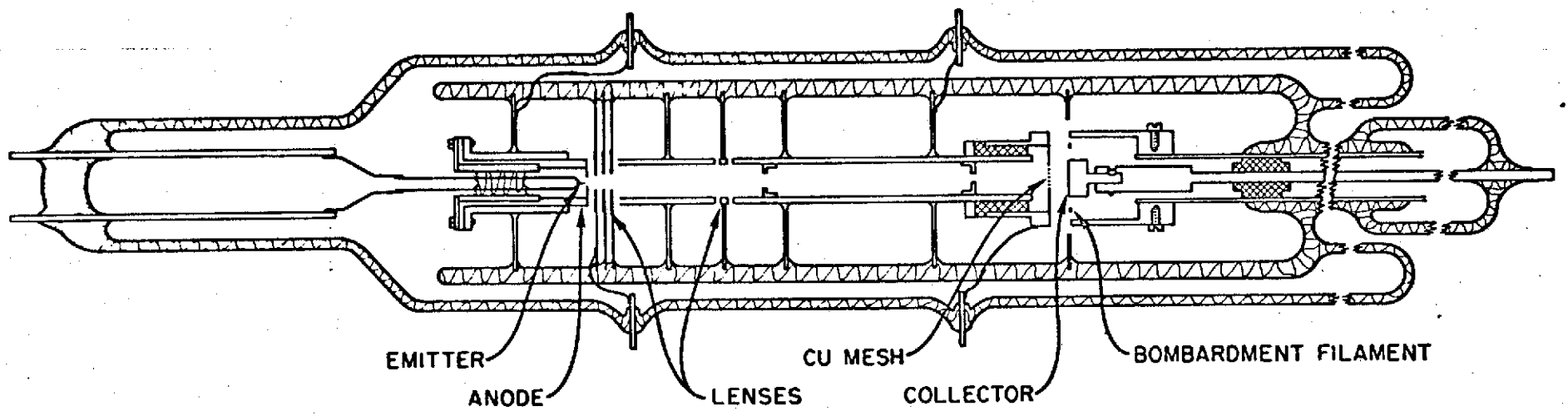
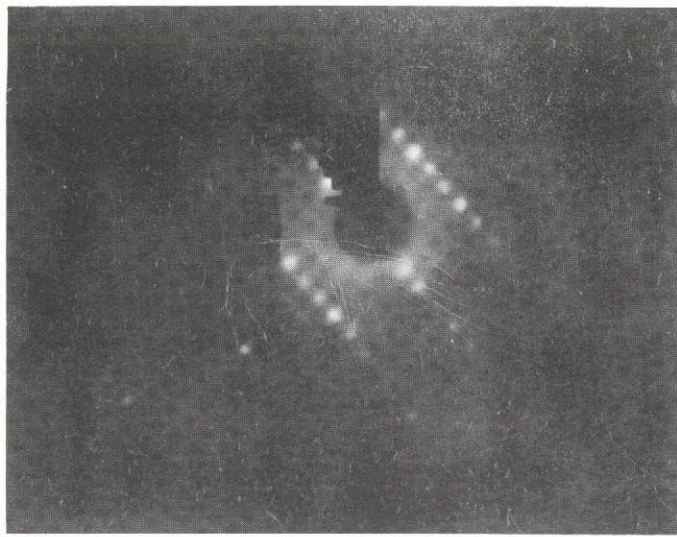
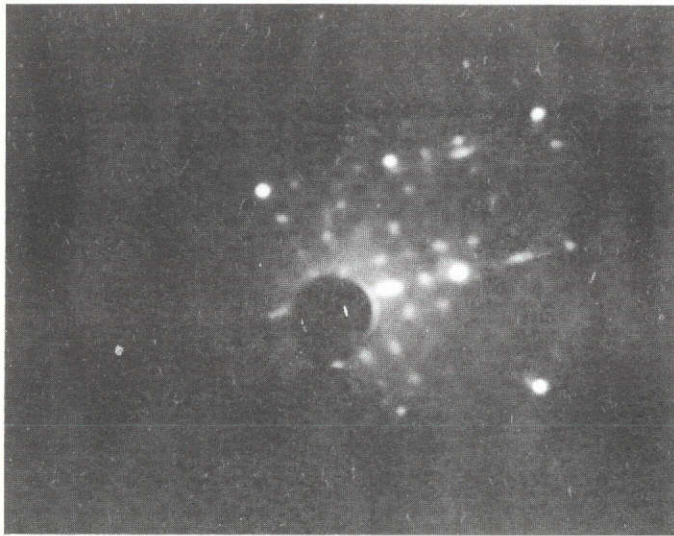


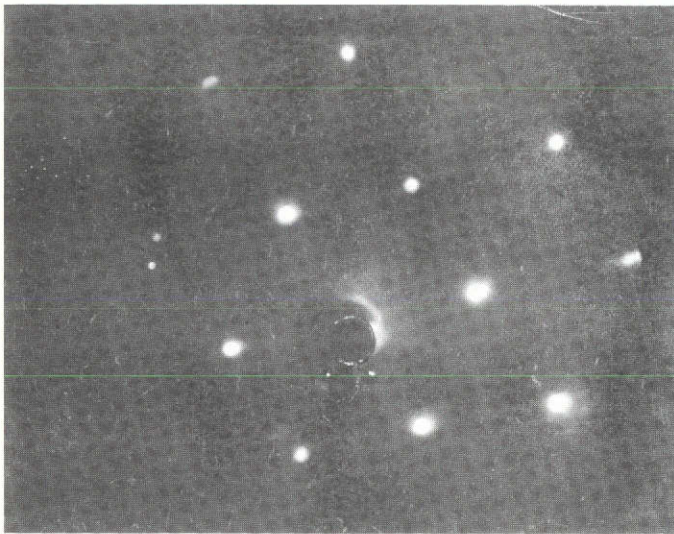
Figure 3



a



b



c

Figure 4

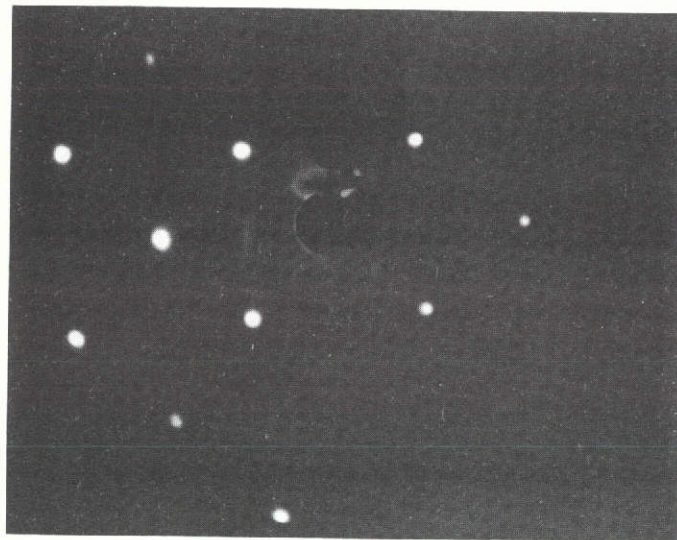
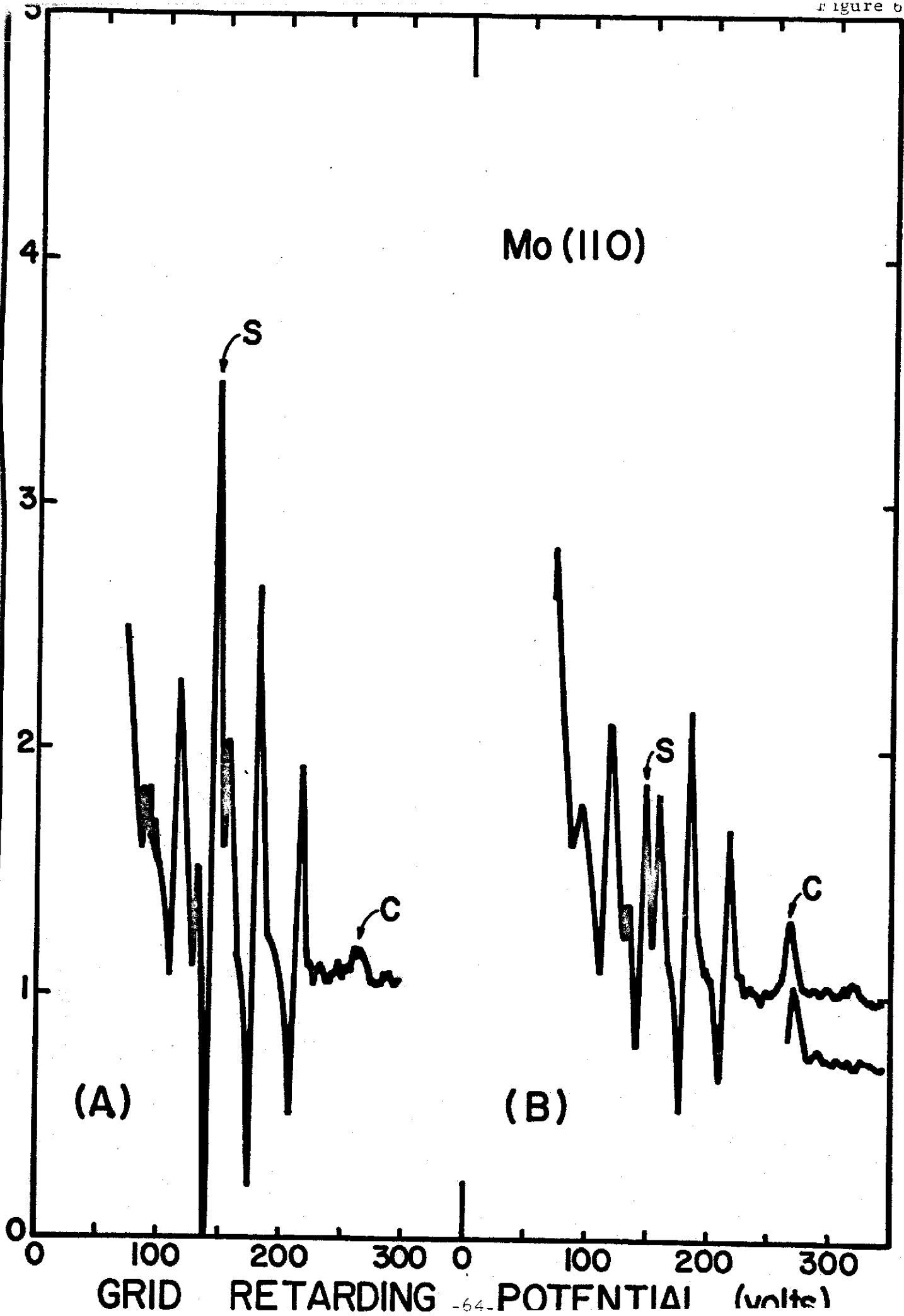
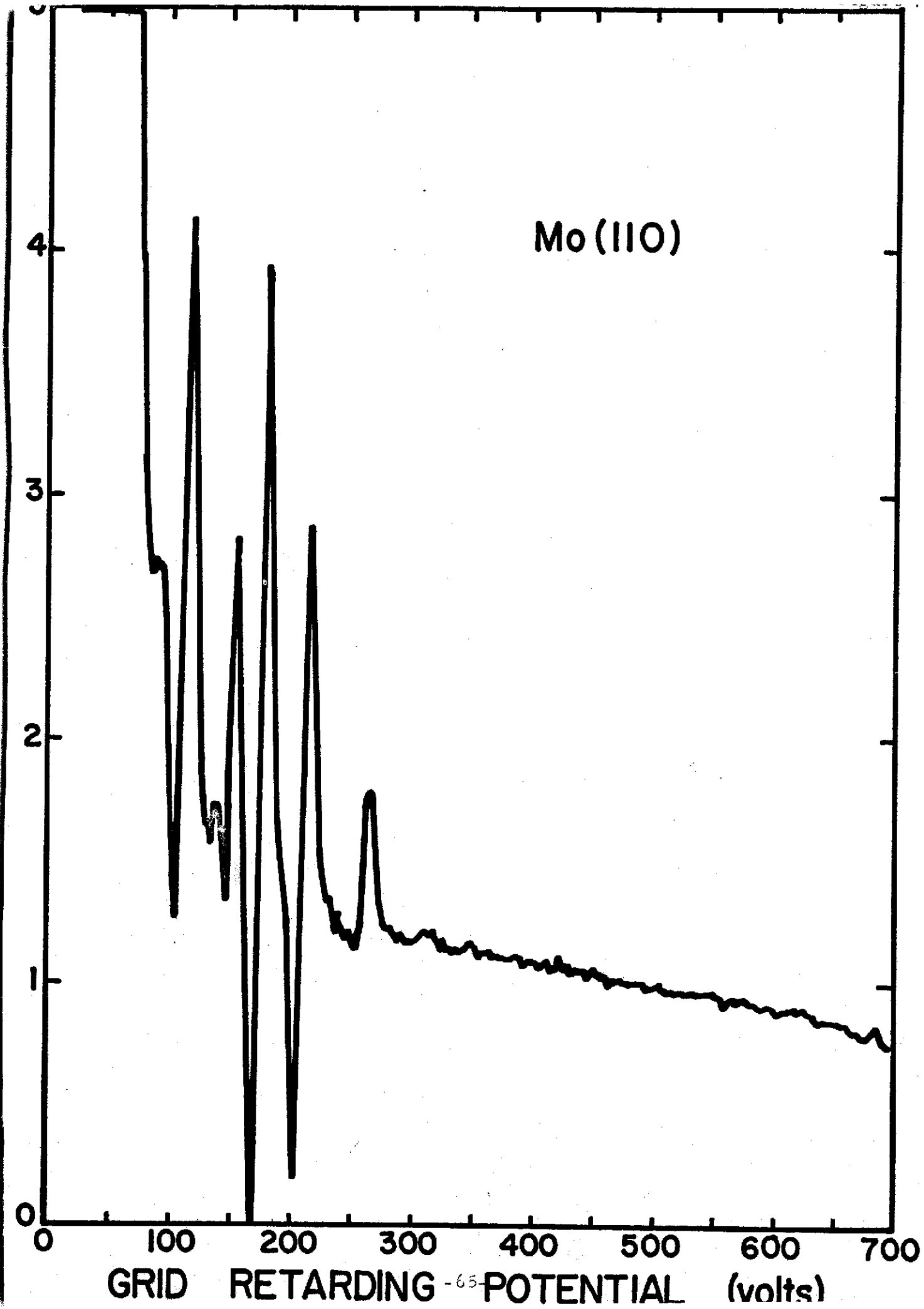
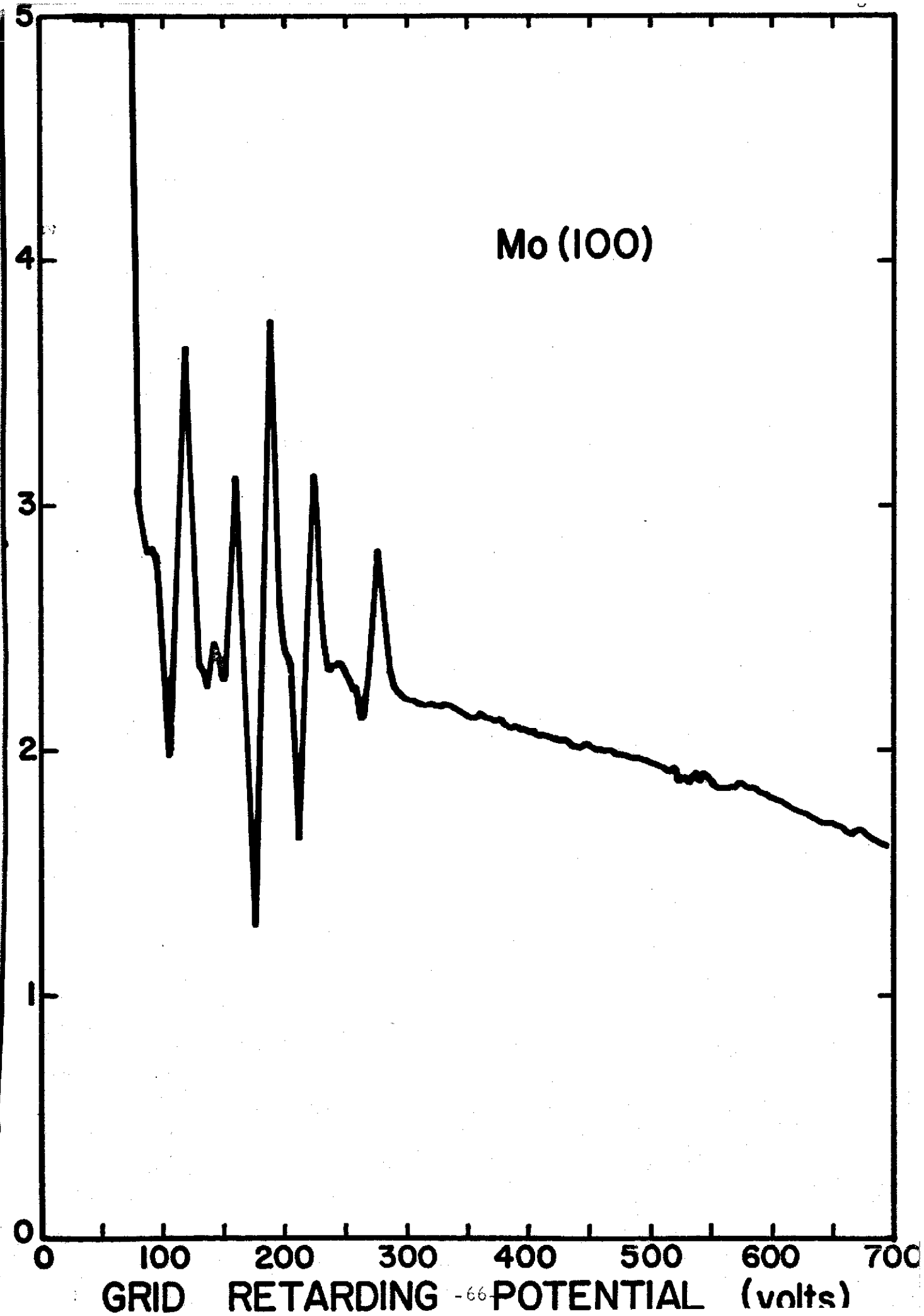
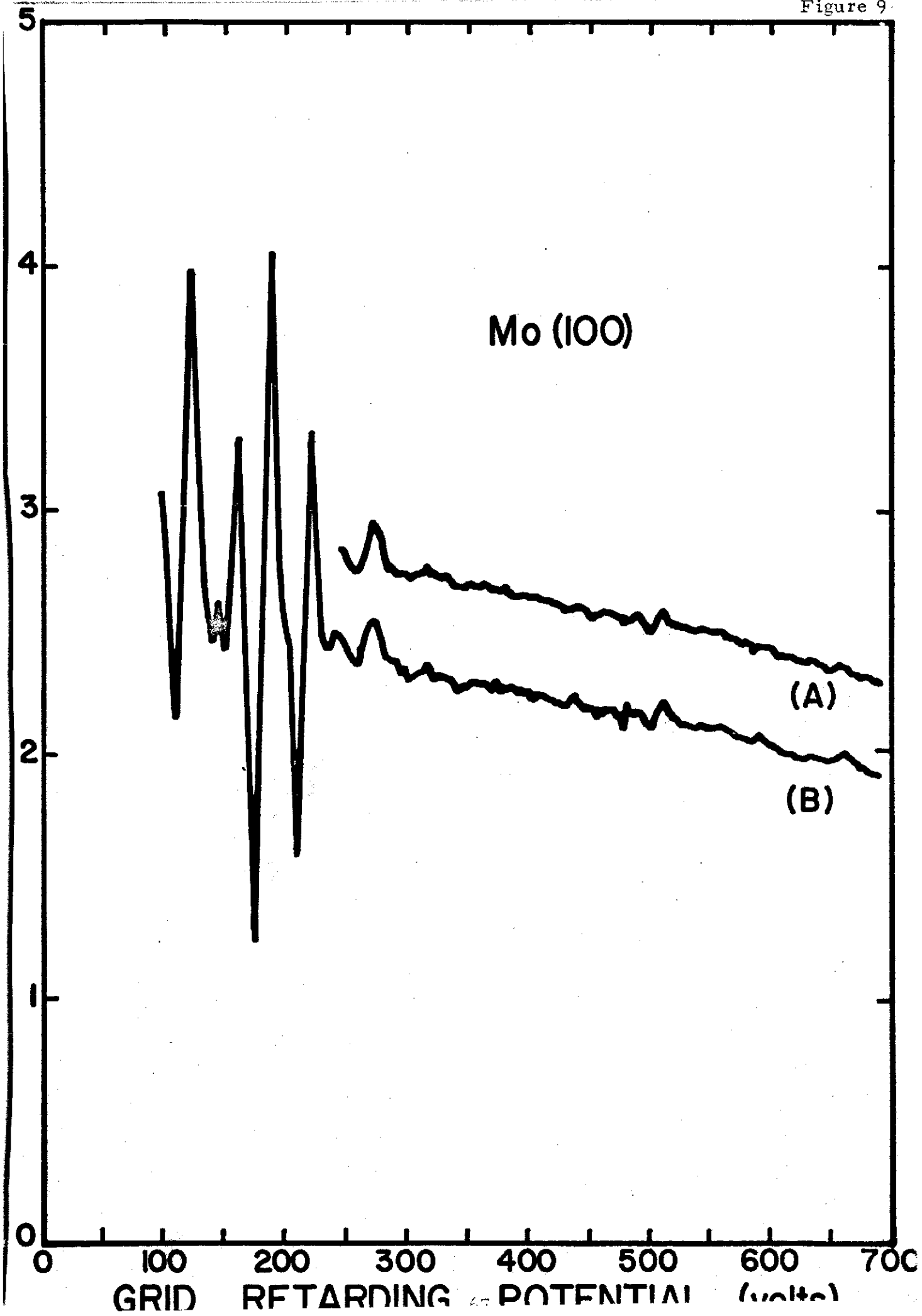


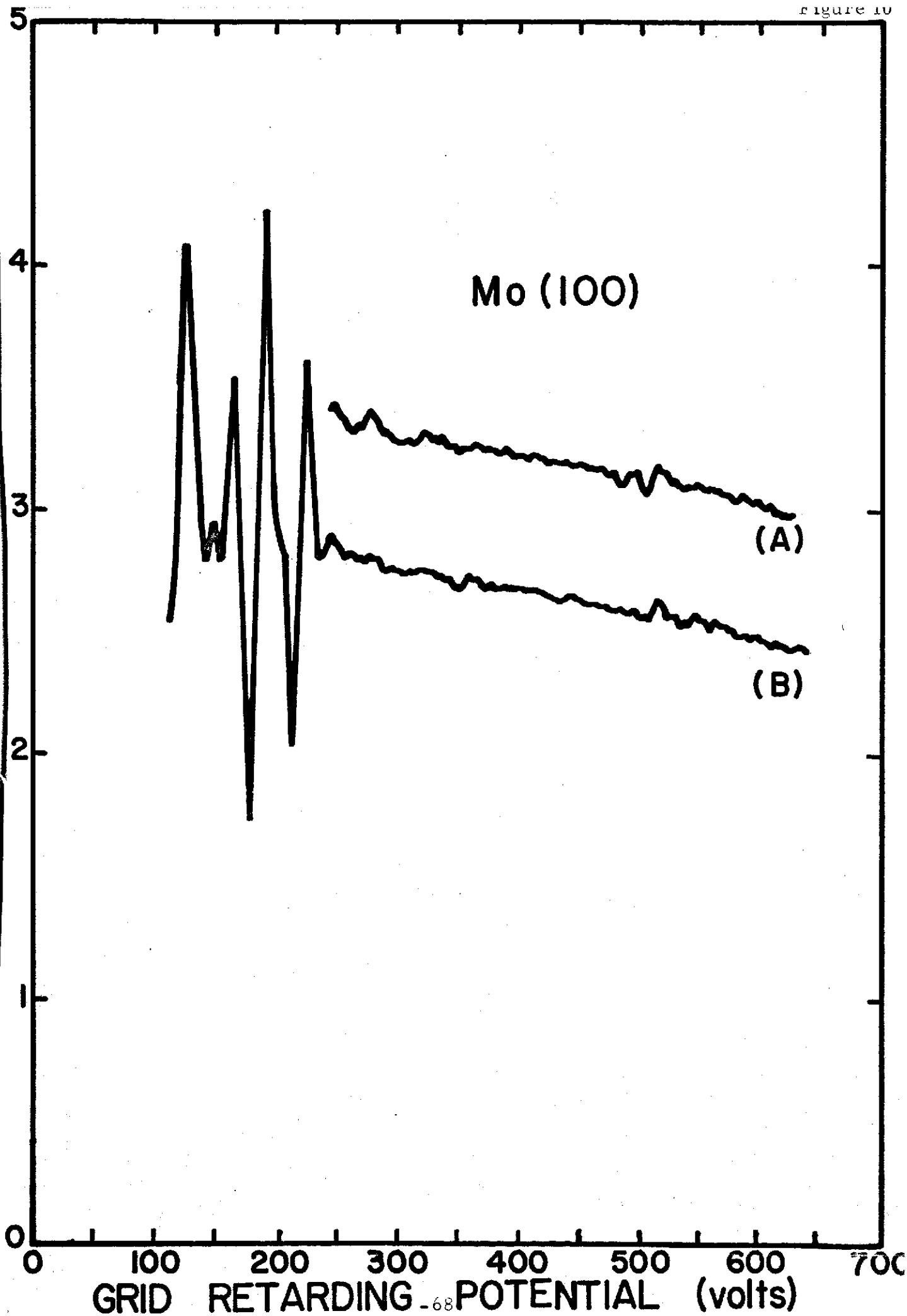
Figure 5











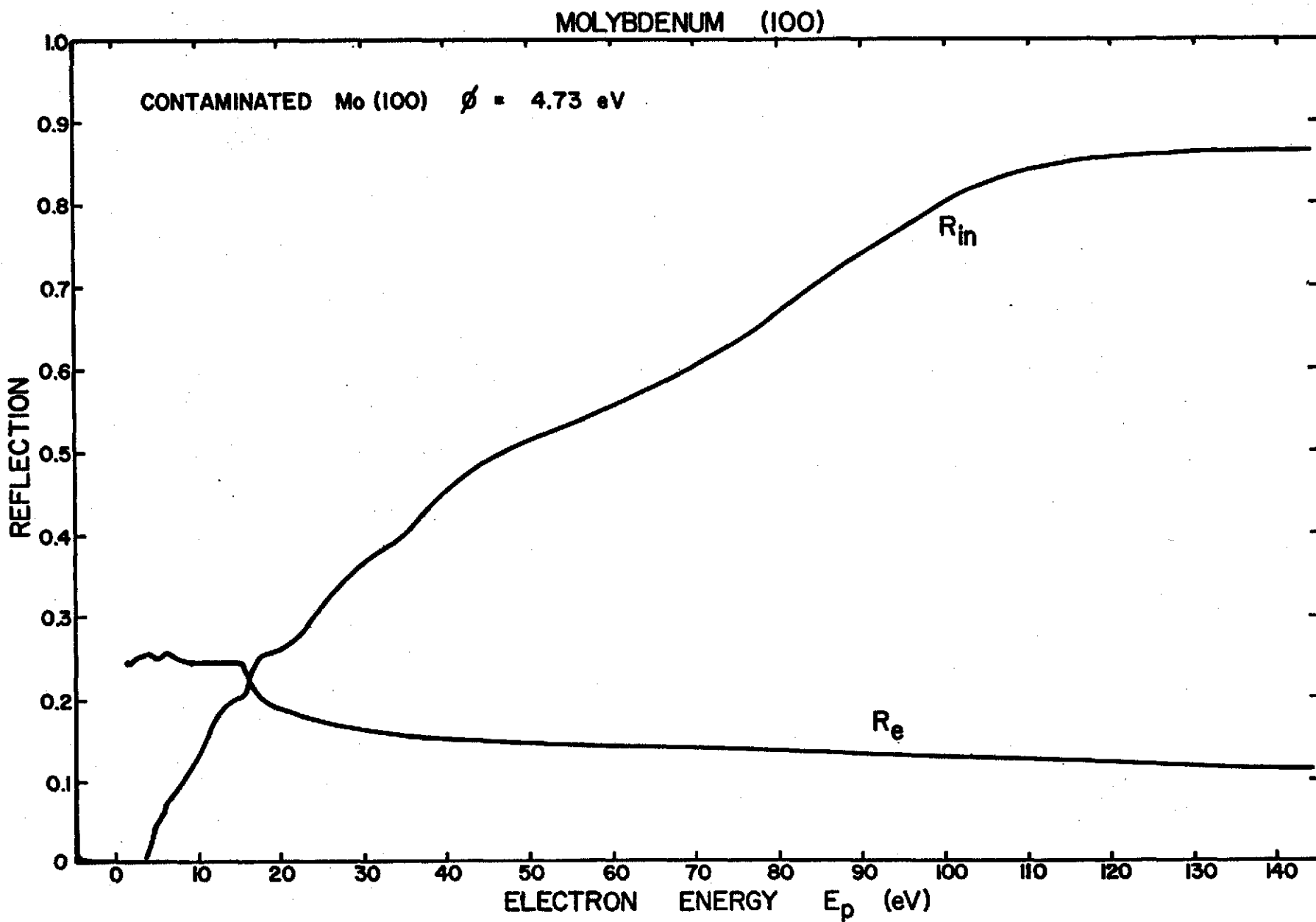
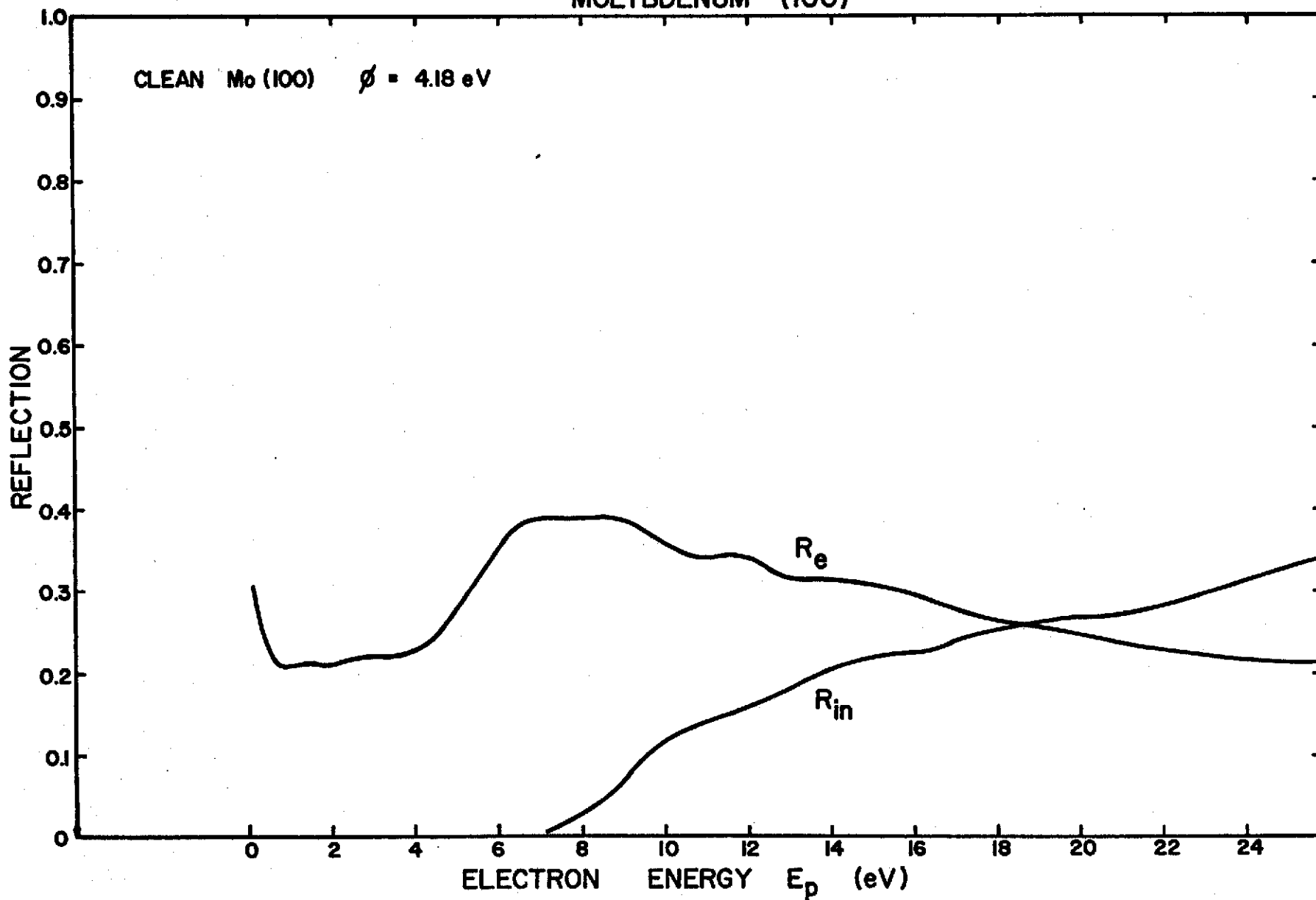


Figure 11

MOLYBDENUM (100)

CLEAN Mo (100) $\phi = 4.18$ eV



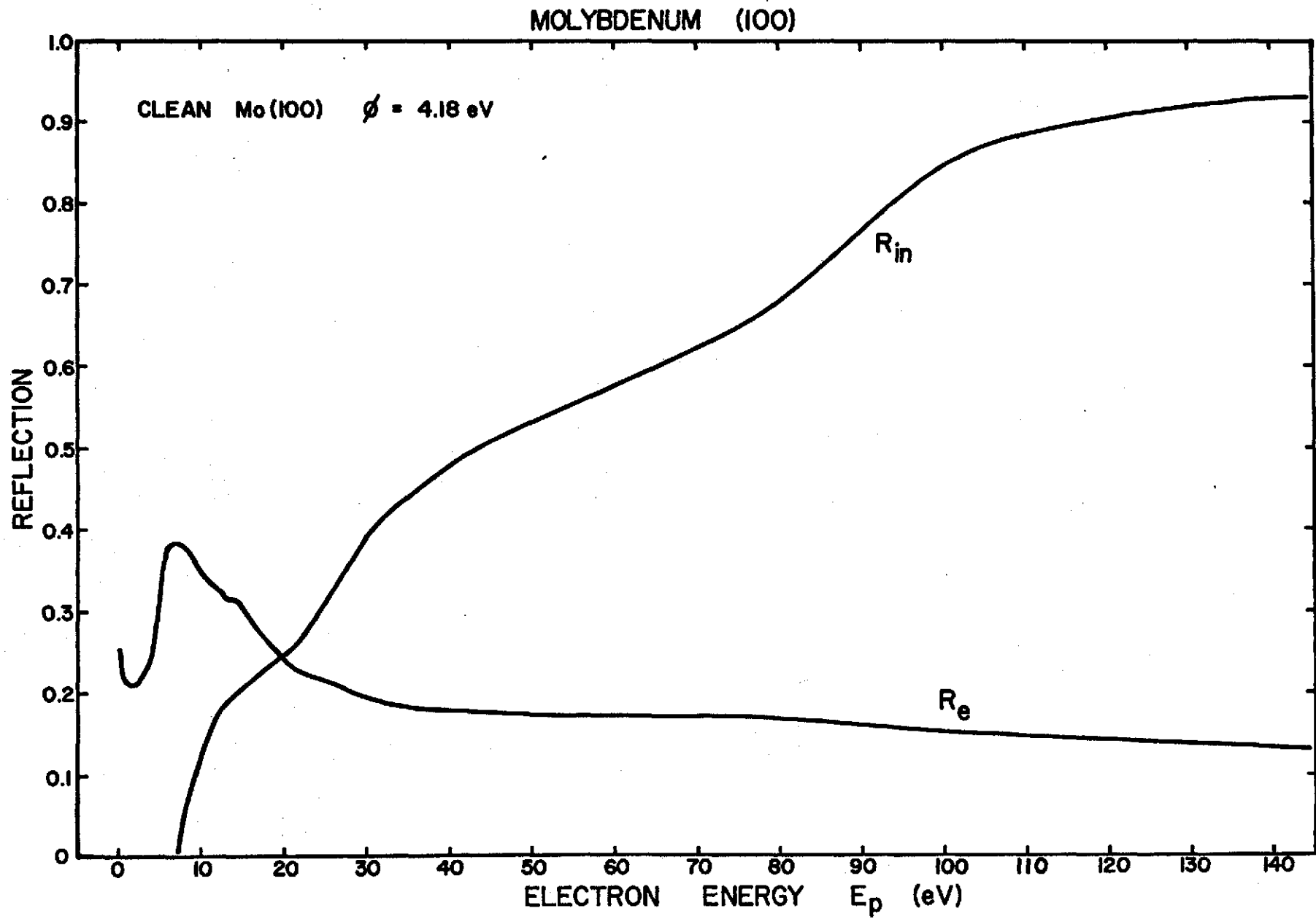


Figure 13

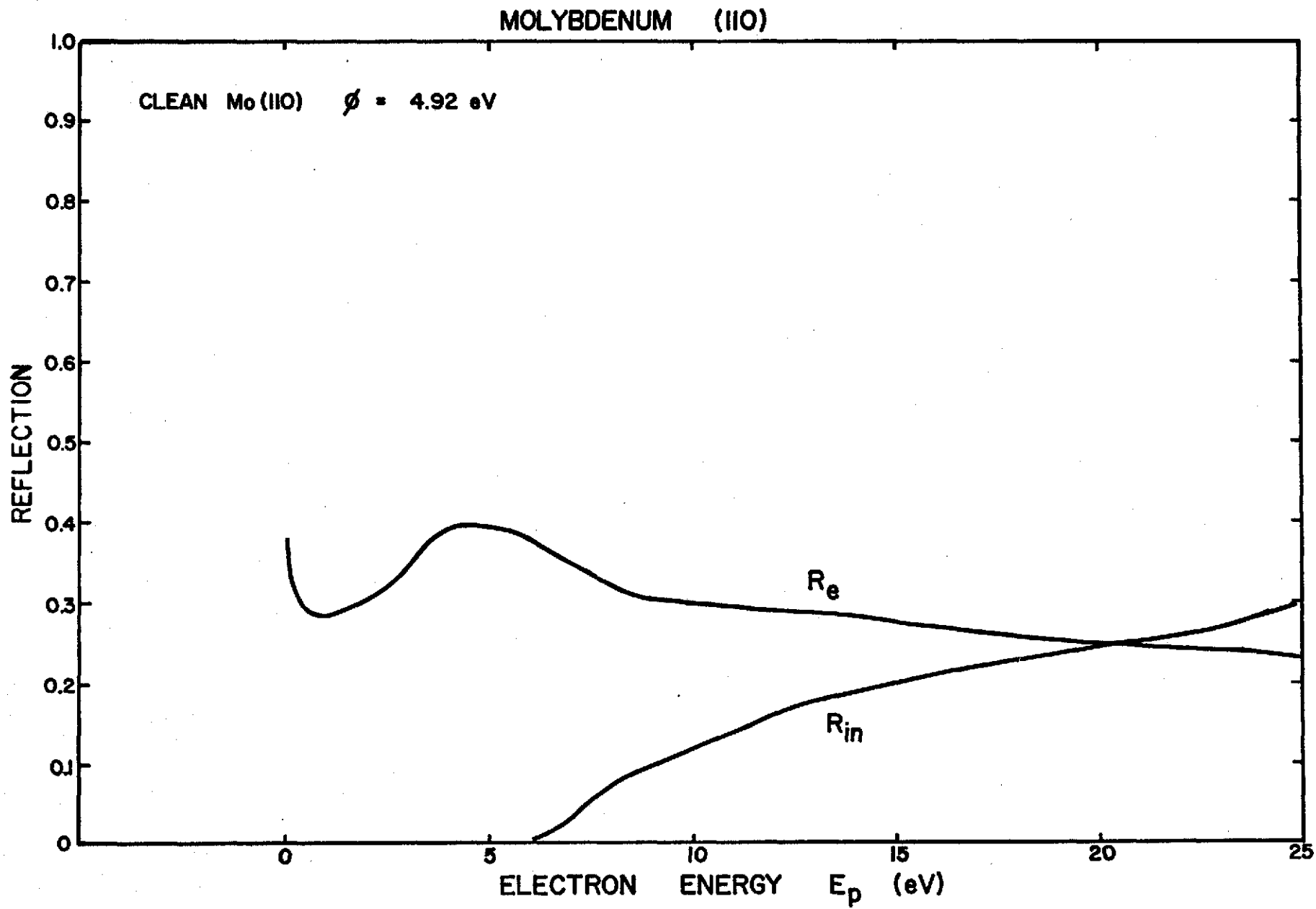


Figure 14

MOLYBDENUM (110)

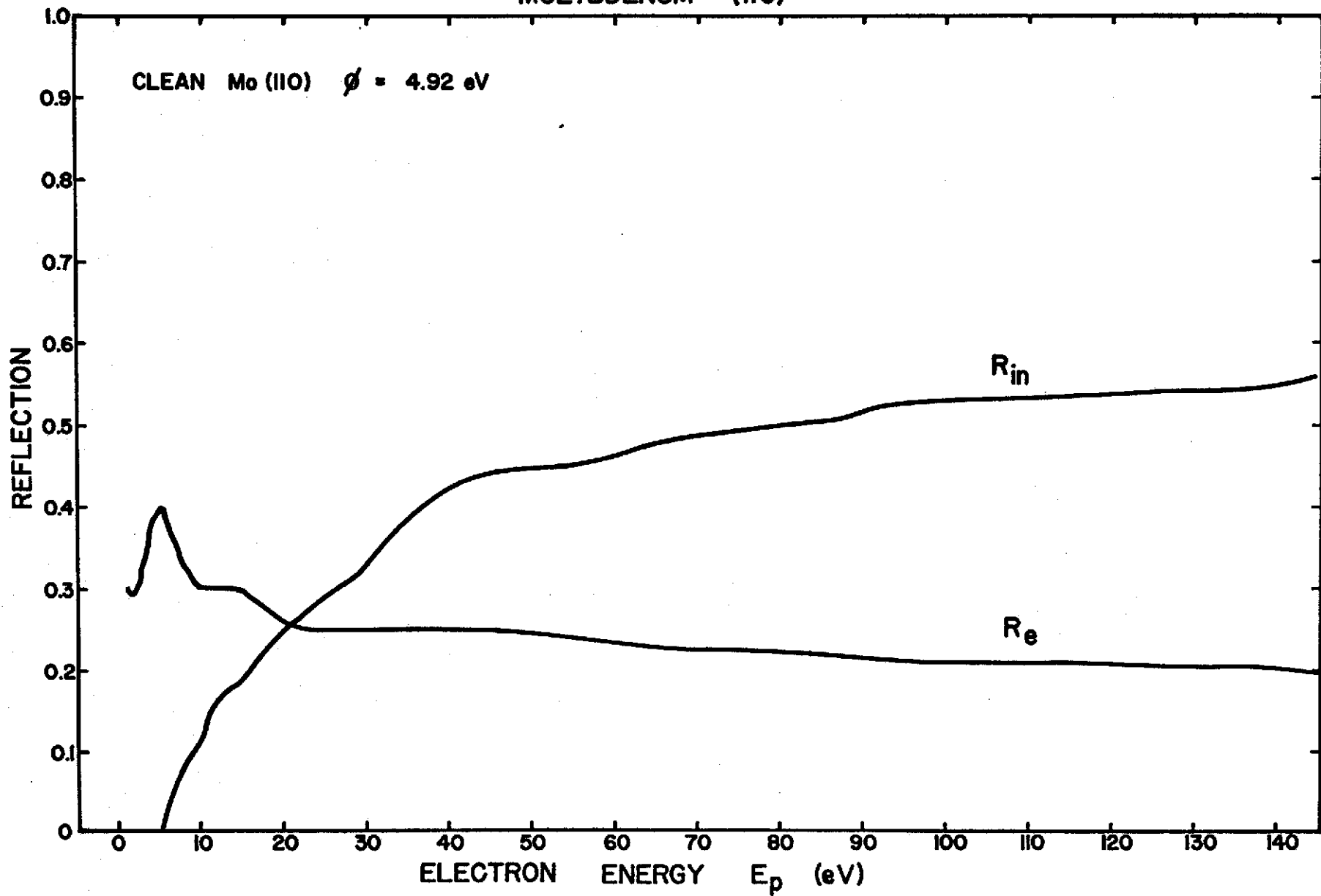


Figure 15